

THE LIMITED IMPACT OF OUTFLOWS: INTEGRAL-FIELD SPECTROSCOPY OF 20 LOCAL AGNs

HYUN-JIN BAE^{1,2}, JONG-HAK WOO^{2,3}, MARIOS KAROUZOS², ELENA GALLO⁴, HELENE FLOHIC⁵, YUE SHEN⁶, AND SUK-JIN YOON¹

¹Department of Astronomy and Center for Galaxy Evolution Research, Yonsei University, Seoul 03722, Republic of Korea; hjbae@galaxy.yonsei.ac.kr

²Astronomy Program, Department of Physics and Astronomy, Seoul National University, Seoul 08826, Republic of Korea; woo@astro.snu.ac.kr

⁴Department of Astronomy, University of Michigan, Ann Arbor, MI 48109-1042, USA

⁵Department of Physics, University of the Pacific, 3601 Pacific Avenue, Stockton, CA 95211, USA and

⁶Department of Astronomy, University of Illinois at Urbana-Champaign, Urbana, IL 61801, USA

Accepted for publication in ApJ (2016/02/06)

ABSTRACT

To investigate AGN outflows as a tracer of AGN feedback on star-formation, we perform integral-field spectroscopy of 20 type 2 AGNs at $z < 0.1$, which are luminous AGNs with the [O III] luminosity $> 10^{41.5}$ erg s⁻¹, and exhibit strong outflow signatures in the [O III] kinematics. By decomposing the emission-line profile, we obtain the maps of the narrow and broad components of [O III] and H α lines, respectively. The broad components in both [O III] and H α represent the non-gravitational kinematics, i.e., gas outflows, while the narrow components, especially in H α , represent the gravitational kinematics, i.e., rotational disk. By using the integrated spectra within the flux-weighted size of the narrow-line region, we estimate the energetics of the gas outflows. The ionized gas mass is $1.0\text{--}38.5 \times 10^5 M_{\odot}$, and the mean mass outflow rate is $4.6 \pm 4.3 M_{\odot} \text{ yr}^{-1}$, which is a factor of ~ 260 higher than the mean mass accretion rate $0.02 \pm 0.01 M_{\odot} \text{ yr}^{-1}$. The mean energy injection rate of the sample is $0.8 \pm 0.6\%$ of the AGN bolometric luminosity, while the momentum flux is $(5.4 \pm 3.6) \times L_{\text{bol}}/c$ on average, except for two most kinematically energetic AGNs with low L_{bol} , which are possibly due to the dynamical timescale of the outflows. The estimated outflow energetics are consistent with the theoretical expectations for energy-conserving outflows from AGNs, yet we find no supporting evidence of instantaneous quenching of star formation due to the outflows.

Keywords: galaxies: active — galaxies: kinematics and dynamics — techniques: imaging spectroscopy

1. INTRODUCTION

The relatively tight scaling relationships between the mass of supermassive black holes (SMBHs) and host galaxy properties suggest SMBH-galaxy co-evolution (for a review, see Kormendy & Ho 2013). Hydro-dynamic simulations show that powerful mechanical and/or radiative feedback from mass accreting SMBHs, or active galactic nuclei (AGN), sweeps a large fraction of interstellar medium (ISM), and therefore regulates the growth of both SMBHs and their host galaxies (Croton et al. 2006; Zubovas & King 2012; Faucher-Giguère & Quataert 2012; Zubovas & Nayakshin 2014; Choi et al. 2015). The AGN feedback is now generally considered as one of the key ingredients of galaxy evolution scenarios, yet it is still unclear how AGN feedback affects the ISM at galactic scales.

AGN-driven gas outflows can be a good tracer of the AGN feedback in action (e.g., Rupke et al. 2005; Greene et al. 2012), as energetic outflows may significantly influence the surrounding ISM and also star formation in host galaxies. Observational studies have shown that gas outflows are prevalent among AGNs based on statistical investigations of the gas kinematics in the narrow-line region (NLR) (e.g., Boroson 2005; Zhang et al. 2011; Wang et al. 2011; Bae & Woo 2014; Woo et al. 2016). Thus, it is important to investigate AGN outflows to understand AGN feedback as well as the SMBH-galaxy co-evolution.

Spectroscopic observations with integral-field units (IFUs) open a new window for studying AGN outflows by providing spatially resolved information on the gas and stellar kinematics. Extensive optical and near-infrared spectroscopic studies have been performed for low- z and high- z AGNs with

IFU over the past decades (e.g., Müller-Sánchez et al. 2011; Greene et al. 2012; Husemann et al. 2013; Liu et al. 2013b; Cicone et al. 2014).

The main purpose of the IFU studies of AGN outflows is to obtain detailed kinematic information of AGNs and their surrounding gas. Extensive studies of nearby Seyfert galaxies have revealed the kinematics of gas outflows in the narrow-line region (NLR) (e.g., Barbosa et al. 2009; Schnorr-Müller et al. 2014; Riffel et al. 2014; Fischer et al. 2015), while other studies focused on the most luminous quasars (or QSOs) at higher z in order to catch the energetic AGN feedback in action (Nesvadba et al. 2006; Rupke & Veilleux 2011; Greene et al. 2012; Liu et al. 2013b; Husemann et al. 2014). These studies have revealed the structure of gas outflows in nearby Seyfert galaxies and probed the energetics of the luminous AGNs, yet there is a lack of systematic investigation on the strong outflows based on a statistical sample, particularly in the local universe at $z < \sim 0.1$.

Recently, Woo et al. (2016, see also Bae & Woo 2014, Woo et al. 2017) performed a census of ionized gas outflows using a large sample of $\sim 39,000$ type 2 AGNs out to $z \sim 0.3$, by investigating the luminosity-weighted velocity and velocity dispersion of the [O III] line at 5007Å. Using the spatially-integrated SDSS spectra, they find that AGN outflows are prevalent among local AGNs. The sample of AGNs with detected gas outflows, particularly with extreme velocities, is very useful for follow-up spatially-resolved studies in investigating the nature of gas outflows and understanding the role of outflows as one of the potential AGN feedback mechanisms. As a pilot study, Karouzos et al. (2016a,b) performed an IFU spectroscopy of six luminous type 2 AGNs using Gemini/GMOS-IFU, successfully demonstrating the power of IFU spectroscopy for studying both gas outflows and star-

³ Author to whom any correspondence should be addressed

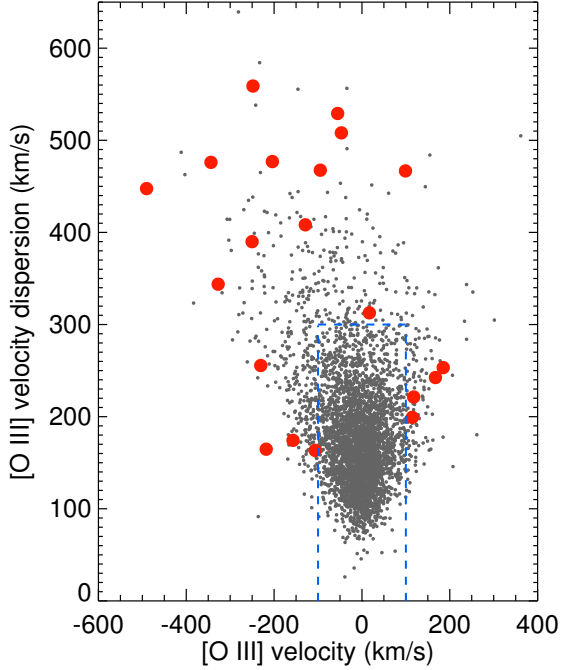


Figure 1. The velocity-velocity dispersion diagram for 3396 luminous ($L_{[\text{O III}],\text{cor}} > 10^{41.5}$ erg s $^{-1}$) type 2 AGNs at $z < 0.1$ (gray dots), and the 20 AGNs observed with IFU (red dots). The blue dashed lines indicate our selection criteria for the AGNs with signs of gas outflows, i.e., $[\text{O III}]$ velocity offset > 100 km s $^{-1}$ or $[\text{O III}]$ velocity dispersion > 300 km s $^{-1}$.

formation in local AGNs.

In this paper, we present the IFU results of a luminosity-limited sample of 20 type 2 AGNs using the Magellan/IMACS-IFU and the VLT/VIMOS-IFU. The sample is selected as the best candidates with extreme gas kinematics from our previous statistical study Woo et al. (2016). By performing emission-line decomposition into narrow and broad components, we try to understand the complex nature of the NLR and its kinematics, and estimate the energetics of the outflows (i.e., energy injection rate, momentum flux, mass outflow rate, and so on) based on simple physical assumptions. In Section 2, we describe the sample selection, observation, and reduction process. In Section 3, we describe the analysis method and 2-D map construction. In Section 4, we present the NLR properties based on $[\text{O III}]$ and $\text{H}\alpha$, respectively, and the size-luminosity relation for the NLR of AGNs. In Section 5, we present the energetics of the gas outflows, and we discuss the results in Section 6. Finally, summary and conclusions follow in Section 7. We adopt a standard Λ CDM cosmology, i.e., $H_0 = 70$ km s $^{-1}$ Mpc $^{-1}$, $\Omega_\Lambda = 0.73$, and $\Omega_m = 0.27$, unless noted otherwise.

2. OBSERVATIONS AND REDUCTION

2.1. Sample Selection

We used the results of the ionized gas kinematics of $\sim 39,000$ type 2 AGNs at $z < 0.3$ from Woo et al. (2016). The study has several advantages as an outflow census of type 2 AGNs. First, Woo et al. (2016) uniformly selected a large number of type 2 AGNs from the SDSS DR7 (Abazajian et al. 2009) using the emission-line diagnostics. Second, they measured the systemic velocity based on the stellar absorption lines, since the systemic velocity provided by the

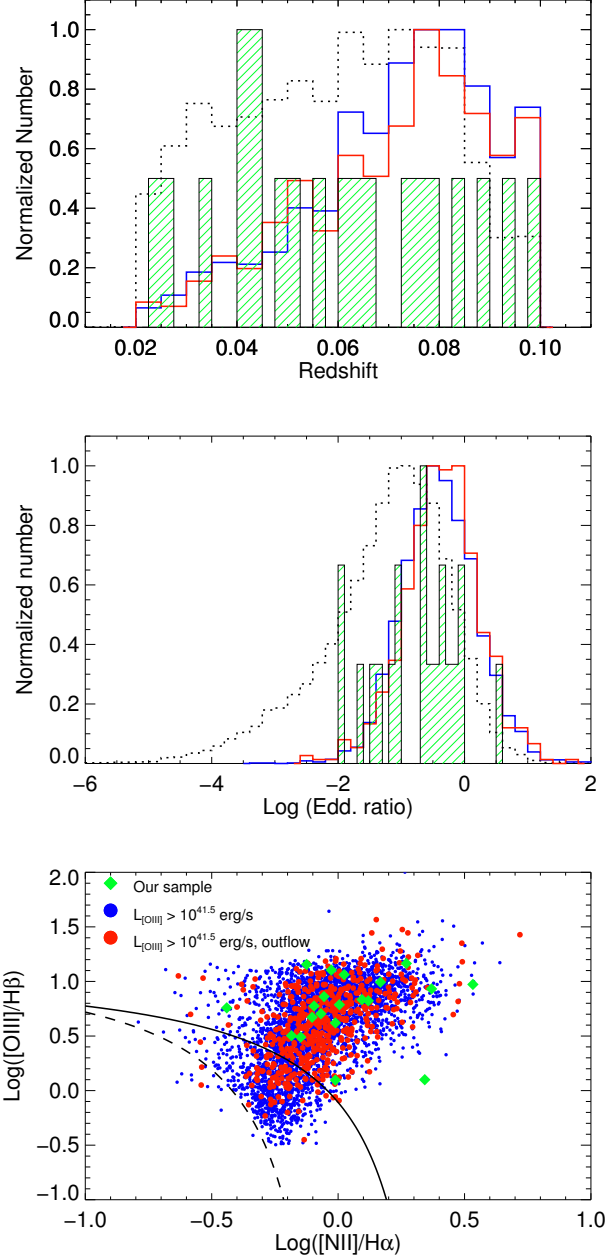


Figure 2. The distributions of redshifts (top) and Eddington ratios (middle) for type 2 AGNs at $z < 0.1$ (dotted line), for the luminosity-limited ($L_{[\text{O III}]} > 10^{41.5}$ erg s $^{-1}$) sample (blue lines), and for the strong outflow AGNs from the luminosity-limited sample (red lines, $v_{[\text{O III}]} > 100$ km s $^{-1}$ and/or $\sigma_{[\text{O III}]} > 300$ km s $^{-1}$). Green histograms represent the distributions of 20 IFU-observed AGNs. The emission-line diagnostic diagram for the samples is at the bottom. The 20 IFU-observed AGNs are denoted with green diamonds.

SDSS pipeline is uncertain due to the fact that redshift measurements are partly based on emission-line features. Third, they provided the ionized gas kinematics by measuring the first moment (velocity) and the second moment (velocity dispersion) of $[\text{O III}]$.

We selected AGNs with strong outflow signatures from the parent sample of Woo et al. (2016) (Figure 1). First, we limited the redshift range to $z < 0.1$ in order to have enough spatial resolution and extent of outflows for given

Table 1
Targets and observations

SDSS name	α_{2000} hh mm ss.s	δ_{2000} dd mm ss	Redshift	$\log L_{[\text{O III}],\text{cor}}$	Class	Obs. date	Telescope/Instrument	seeing	t_{exp}
(1)	(2)	(3)	(4)	(5)	(6)	(7)	(8)	(9)	(10)
J0130+1312	01 30 37.8	+13 12 52	0.07272	42.01	S	2014 Dec 26	Magellan/IMACS-IFU	0.9	2400
J0341-0719	03 41 34.9	-07 19 25	0.06603	41.90	S	2014 Dec 26	Magellan/IMACS-IFU	0.7	7200
J0806+1906	08 06 01.5	+19 06 15	0.09799	42.34	S	2014 Dec 26	Magellan/IMACS-IFU	0.8	3600
J0855+0047	08 55 47.7	+00 47 39	0.04185	41.63	S	2013 Apr	VLT/VIMOS-IFU	1.0	10050
J0857+0633	08 57 59.0	+06 33 08	0.07638	41.74	S	2014 Apr 06	Magellan/IMACS-IFU	1.0	7200
J0911+1333	09 11 24.2	+13 33 20	0.07966	42.17	S	2014 Dec 27	Magellan/IMACS-IFU	0.8	5400
J0952+1937	09 52 59.0	+19 37 55	0.02445	41.52	S	2014 Apr 05	Magellan/IMACS-IFU	1.0	3600
J1001+0954	10 01 40.5	+09 54 32	0.05638	42.11	S	2014 Apr 06	Magellan/IMACS-IFU	1.0	5400
J1013-0054	10 13 46.8	-00 54 51	0.04258	42.18	S	2014 Apr 04	Magellan/IMACS-IFU	1.0	3600
J1054+1646	10 54 23.8	+16 46 53	0.09498	42.39	L	2014 Apr 27	Magellan/IMACS-IFU	0.7	7200
J1100+1321	11 00 03.9	+13 21 50	0.06420	42.10	S	2014 Dec 26	Magellan/IMACS-IFU	0.8	7200
J1100+1124	11 00 37.2	+11 24 55	0.02700	40.88	S	2013 Apr	VLT/VIMOS-IFU	0.8	8040
J1106+0633	11 06 30.7	+06 33 34	0.04044	41.90	S	2013 Apr	VLT/VIMOS-IFU	0.8	8040
J1147+0752	11 47 20.0	+07 52 43	0.08271	42.33	L	2014 Dec 28	Magellan/IMACS-IFU	0.9	7200
J1214-0329	12 14 51.2	-03 29 22	0.03382	42.41	S	2014 Apr 04	Magellan/IMACS-IFU	0.7	3600
J1310+0837	13 10 57.3	+08 37 39	0.05211	41.76	S	2014 Apr 04	Magellan/IMACS-IFU	1.0	3600
J1440+0556	14 40 18.0	+05 56 34	0.06105	42.45	S	2014 Apr 06	Magellan/IMACS-IFU	1.1	5400
J1448+1055	14 48 38.5	+10 55 36	0.08930	42.83	S	2014 Apr 06	Magellan/IMACS-IFU	1.3	5400
J1520+0757	15 20 33.7	+07 57 12	0.04343	41.11	S	2014 Apr 06	Magellan/IMACS-IFU	1.3	5400
J2039+0033	20 39 07.0	+00 33 16	0.04835	42.15	S	2014 May 21	Magellan/IMACS-IFU	1.0	10800

Note. — (1) SDSS name of AGN; (2) Right ascension (J2000); (3) Declination (J2000); (4) Redshift derived from the brightest spaxel of observed spectra; (5) Extinction-corrected [O III] luminosity in logarithm (erg s^{-1}); (6) Class from the emission-line diagnostics, i.e., Seyfert (S), & LINER (L); (7) Date of observation (local); (8) Telescope and instrument; (9) Seeing size ($''$); (11) Exposure time (second).

the IFU field-of-view (FoV). Then, we selected 3396 AGNs ($\sim 9\%$) with a relatively high dust-corrected [O III] luminosity ($\log L_{[\text{O III}],\text{cor}} > 41.5 \text{ erg s}^{-1}$) since the outflow fraction increases with the [O III] luminosity (e.g., [Bae & Woo 2014](#); [Woo et al. 2016](#),?). We further selected 491 AGNs ($\sim 14\%$ of the luminosity-limited sample) with strong outflow signatures in [O III] kinematics, i.e., [O III] velocity offset $v_{[\text{O III}]}$ $> 100 \text{ km s}^{-1}$, or [O III] velocity dispersion $\sigma_{[\text{O III}]} > 300 \text{ km s}^{-1}$. The selected AGNs are only $\sim 1\%$ of the parent sample, consisting of the best candidates for outflow studies with local AGNs. Among the selected AGNs, we observed 18 AGNs with IFUs (see Table 1). Note that we observed 2 additional targets (J1100+1124 and J1520+0757), which satisfy the selection criteria for gas kinematics but with a slightly lower [O III] luminosity ($L_{[\text{O III}],\text{cor}} \sim 10^{41} \text{ erg s}^{-1}$). We also note that the AGNs presented in the pilot study by [Karouzos et al. \(2016a,b\)](#) is a subsample with stronger outflow signatures than ours (e.g., $L_{[\text{O III}],\text{cor}} > 10^{42.0} \text{ erg s}^{-1}$).

We calculate the AGN bolometric luminosity L_{bol} as $\log L_{\text{bol}} = 3.8 + 0.25 \log L_{[\text{O III}],\text{cor}} + 0.75 \log L_{[\text{O I}],\text{cor}}$, where $L_{[\text{O I}],\text{cor}}$ is the extinction-corrected [O I] $\lambda 6300$ luminosity ([Netzer 2009](#)). We infer the black hole mass (M_{BH}) by adopting the $M_{\text{BH}} - \sigma_*$ relation ([Park et al. 2012](#)), where σ_* is the stellar velocity dispersion obtained from the MPA-JHU catalog of SDSS DR7². We find that AGNs with strong outflows show no significant difference in the distributions of redshift, Eddington ratio, and the emission-line ratios (e.g., [Baldwin et al. 1981](#)), compared to the AGNs in the luminosity-limited sample (Figure 2). Thus, we assume that the selected AGNs are a random sub-sample of the luminosity-limited sample.

2.2. Magellan/IMACS-IFU Observations & Reduction

We observed 17 out of 20 type 2 AGNs with the IFU of the Inamori Magellan Areal Camera (IMACS-IFU) on the Magellan telescope at Las Campanas Observatory. We used the $f/4$ (long mode) camera with a recently upgraded Mosaic 3 CCD ($8\text{k} \times 8\text{k}$). We used the 300 lines/mm grating with a tilt angle

of 6.0° , providing a large wavelength range of 3420-9550 \AA with a spectral resolution $R \approx 1600$. The choice of $f/4$ camera provides an FoV of $5'' \times 4.5''$ with 600 fibers, and each spaxel (spatial pixel) has a size of $0.2''$ in diameter on the sky. Given the range of redshift of our targets, we explore the central region within a several kpc from the nucleus, which provides detailed information on the gas outflows in the central region of the host galaxies.

The observations were performed during 7 nights in April, May, and December 2014 with a seeing $0.7'' - 1.3''$ in April and May, and $0.7'' - 0.9''$ in the December run. In each afternoon, we obtained bias images, HeNeAr arcs, dome flats, and sky flats if possible. During the night, we initially took an acquisition image with the IFU to make sure the target was located at the center of the FoV. During our first run (April 6), however, the acquisition was poorly performed due to an unexpected spatial offset of the IFU images on the CCD. Hence the targets of the night failed to be located at the center of the FoV. For the other nights, after locating the target at the center of the FoV, we took science exposures and an arc image at the same position of the telescope. For each observing run, we observed spectrophotometric standard stars for flux calibration.

For the IMACS-IFU data reduction, we utilized an IDL-based software P3D³, which is a general-purpose data reduction tool for fiber-fed IFUs ([Sandin et al. 2010](#)). Since P3D does not officially support the IMACS-IFU data reduction yet, we modified the parameter files in the code for the IMACS-IFU instrument setup. First, we constructed a master bias frame then subtracted the bias frame from all exposures. We also constructed a combined dome flat image with the IFU as a reference frame for tracing of the dispersed light. Using the combined dome flat image, we obtained a tracing solution for each target. Since we did not obtain a dome flat image after each science exposure, we manually shifted the dome flat image for each science exposure to properly trace the dispersed light. The shift is, on average, ~ 5 pixels on the CCD

² <http://www.mpa-garching.mpg.de/SDSS/>

³ <http://p3d.sourceforge.net>

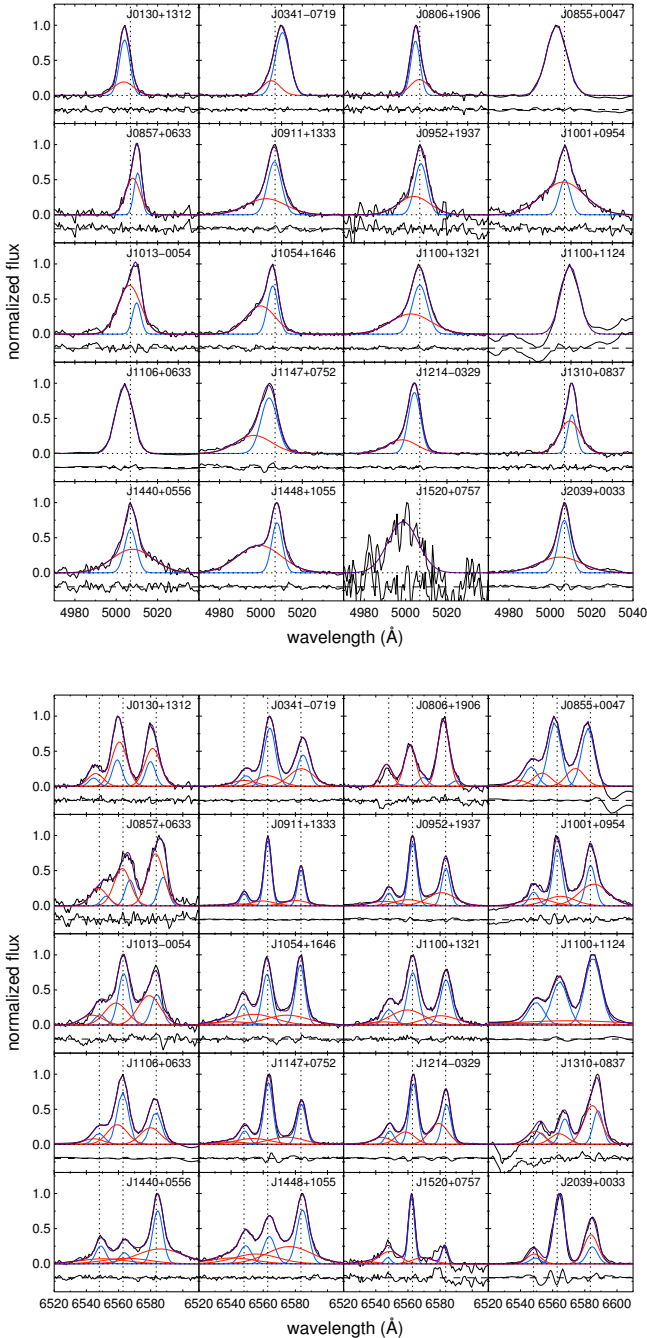


Figure 3. The kinematic decompositions for the [O III] (top panel) and H α lines (bottom panel) based on the integrated spectra of 20 AGNs within the NLR size (R_{NLR} , see Section 4.3). The black thick lines are the residual spectra after stellar-component subtraction from the raw spectra. The red (blue) lines show the broad (narrow) component of the line profile, while the purple lines show the total (narrow+broad) profile. The black thin lines below the spectrum are the difference between the residual spectra and the best-fit models. The AGNs are listed in ascending R.A from top-left to bottom-right. We note that J1520+0757 has a noisy spectrum due to bad weather conditions during the observation of the target.

in the cross-dispersion direction (y-axis). After we obtained the individual tracing solutions, we applied the solution to the HeNeAr arc frame obtained after each target in order to get a wavelength solution. We used a fifth order polynomial function to obtain the wavelength solution, resulting in a residual

r.m.s. of $\sim 0.02\text{\AA}$.

Then we removed cosmic rays on each science frame by using the PyCosmic routine, developed for a robust cosmic-ray removal of fiber-fed IFU data (Husemann et al. 2012). After the cosmic-ray removal, we extracted the object and sky spectra by using the tracing solutions. Among several methods for spectrum extraction, we used the modified optimal extraction with a predefined Gaussian function from the tracing solution, which gives less noise in spectra and more robust results than the top-hat extraction. (Horne 1986; Sandin et al. 2010). IMACS has an internal atmospheric dispersion corrector, hence we did not correct the atmospheric dispersion during the reduction as we do not find any wavelength-dependent spatial offset in the final constructed image. After the spectra extraction, we obtained a mean spectrum of sky background by using dedicated sky fibers, and subtracted the mean sky spectrum from each science spectrum. Finally, we combined all science exposures and calibrated the flux with a sensitivity function obtained from standard star observations. In addition, to increase the signal-to-noise ratio (S/N) in the outskirts of the FoV, we binned 7 adjacent spaxels into a single spectrum. Since the combined spaxels have a size of $0''.6$ in diameter on the sky, we still have spaxels smaller than the seeing ($0''.7\text{--}1''.3$) during the observing runs.

2.3. VLT/VIMOS-IFU Observations & Reduction

For 3 out of 20 AGNs, we obtained the data with the multi-purpose optical instrument VIMOS in IFU mode on the VLT-UT3 (Program ID: 091.B-0343(A), PI: Flohic). We used the MR grating with the GG475 filter, providing a spectral range of $4900 - 10150\text{\AA}$ with a spectral resolution of ~ 720 . The VIMOS-IFU has 6400 fibers (80×80) without dedicated sky fibers. With the adjustable scales of $0.67''$ per fiber, we have a large FoV of $27''\times 27''$, which is a factor of ~ 30 larger than our IMACS-IFU FoV. Thus, the VIMOS-IFU data allowed us to investigate the impact of gas outflows on galactic scales of ~ 10 kpc for the redshift range of our targets. The observing run was executed as a service-mode observation in April 2013. The exposure time was ~ 2.8 hours per target, with 15×670 seconds exposures. We applied a spatial offset of $\pm 2''$ for science exposures to compensate for dead/bad fibers in the array.

The reduction for the VLT/VIMOS-IFU data was performed with P3D in the same manner as the IMACS-IFU data. After that, we combined the multiple exposures by considering the spatial offset of $\pm 2''$. For both J1100+1124 and J1106+0633, we discarded three exposures that suffered from a wrong spatial offset during the observations.

3. ANALYSIS

3.1. Emission-line properties

For each spaxel, we measured the flux and velocities of emission lines after subtracting stellar continuum, as similarly performed by Woo et al. (2016). For stellar continuum, we utilized the pPXF code (Cappellari & Emsellem 2004) to construct the best-fit model using the MILES simple stellar population models with solar metallicity (Sánchez-Blázquez et al. 2006). In this procedure we measured the velocity of the stellar component in each spaxel.

Then, we fit the narrow emission-lines, e.g., the Balmer lines, [O III] $\lambda 5007$, [N II]-doublet, and [S II]-doublet, by utilizing the MPFIT code (Markwardt 2009). Since AGNs with gas outflows generally show a broad wing component, espe-

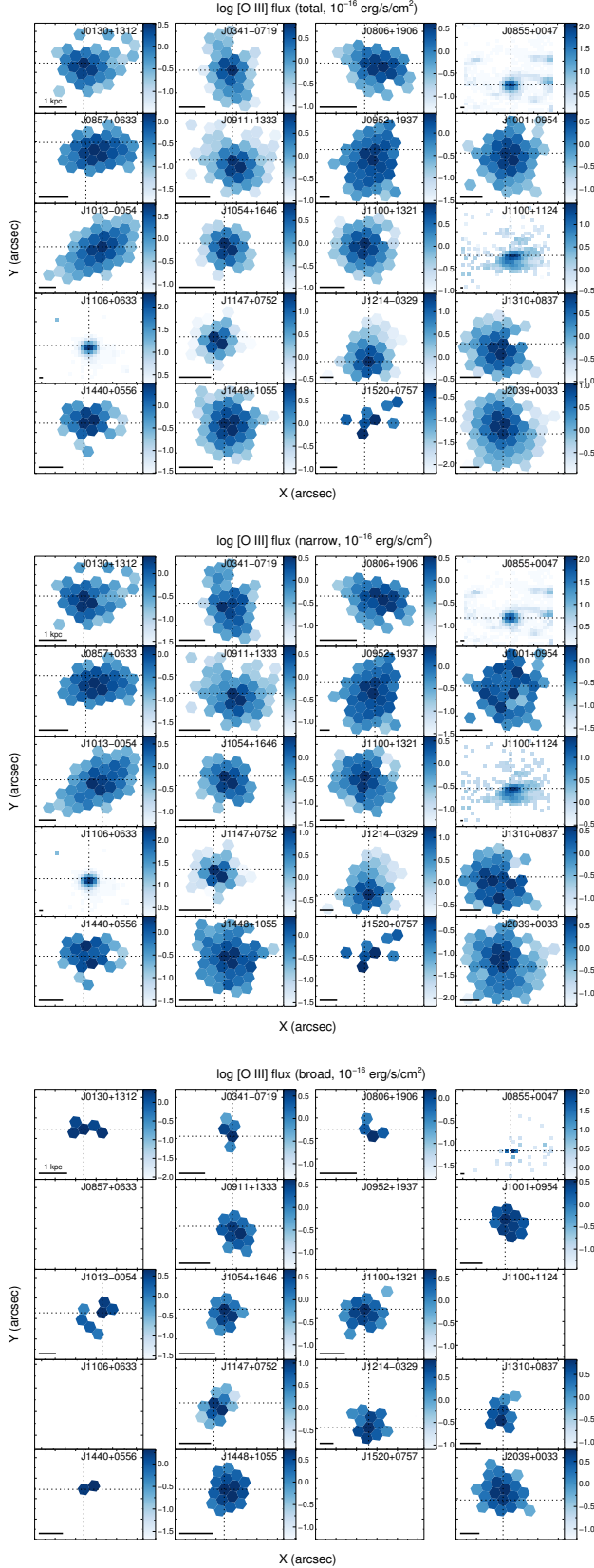


Figure 4. The [O III] flux maps for the total (top panel), the narrow (middle panel), and the broad component (bottom panel). Blank maps for the broad component indicate no detection of the AGNs. The major ticks in both x- and y-axes represent $1''$ for the Magellan targets, while the major ticks denote $5''$ for the VLT targets. The AGNs are listed in order of ascending R.A. from top-left to bottom-right.

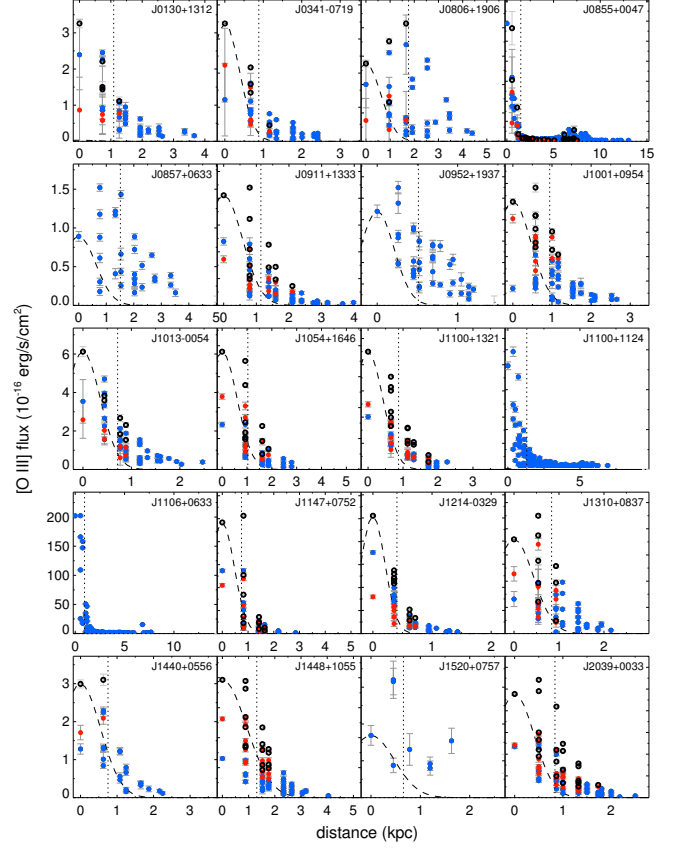


Figure 5. The radial flux distributions of [O III]. Dotted lines in the vertical direction indicate the effective radius of the NLR based on [O III]. The dashed curves show the point-spread-function based on the seeing size. Each panel contains the radial distributions of the narrow component (blue), the broad component (red), if it exists, and the total (narrow+broad) component (black) with 1σ uncertainties.

cially in the [O III] line profile (Greene & Ho 2005; Mullany et al. 2013; Shen & Ho 2014; Woo et al. 2016), we used two Gaussian functions to represent the broad and the narrow components. For the $H\alpha + [N II]$ region, we assumed that each narrow and broad wing component of $H\alpha$ and $[N II]$ has the same kinematics, i.e., velocity and velocity dispersion. We also fixed the flux ratio of $[N II]\lambda 6549$ and $[N II]\lambda 6583$ as one third for both broad and narrow components (Figure 3).

To ensure that the broad component is not fitting the noise in the spectrum, we adopted two conditions for accepting the broad wing component. First, the peak amplitude of the broad component should be a factor of three larger than the standard deviation of the residual spectra at $5050 - 5150\text{\AA}$. For the $H\alpha + [N II]$ region, we choose a larger amplitude of either $H\alpha$ or $[N II]$ broad component as the peak amplitude. Second, the sum of the width (σ) of the two Gaussian components should be smaller than the distance between the peaks of the two Gaussian components. If the broad component is not detected in the fitting, we alternatively fit the emission lines with a single Gaussian function.

Based on the model fit of the emission lines, we calculated the first moment λ_0 and the second moment σ_{line} of each emission line, which respectively represent the luminosity-weighted velocity and velocity dispersion of the emission line,

as

$$\lambda_0 = \frac{\int \lambda f(\lambda) d\lambda}{\int f(\lambda) d\lambda}, \quad (1)$$

$$\sigma_{\text{line}}^2 = \frac{\int \lambda^2 f(\lambda) d\lambda}{\int f(\lambda) d\lambda} - \lambda_0^2, \quad (2)$$

where $f(\lambda)$ is the flux at each wavelength λ . We calculated the velocity shift of emission lines by comparing the first moment and the systemic velocity measured from the center of host galaxies. The second moment was corrected for the instrumental resolution measured from the sky emission lines. To estimate the uncertainties for the measurement, we adopted a Monte Carlo realization generating 100 mock spectra by randomizing the flux with noise, and obtained the measurements from each spectrum. Then we adopted 1σ dispersion of the distribution of each measurement as the uncertainty.

4. THE NARROW-LINE REGION PROPERTIES

In this section, we present the NLR properties based on the spatial distributions of [O III] (Section 4.1) and $H\alpha$ flux and kinematics (Section 4.2). Then we examine the sizes of the NLR and outflows and the size-luminosity relationship (Section 4.3).

4.1. the [OIII]-emitting region

4.1.1. Morphology

We perform a visual inspection of the spatial distribution of the [O III] flux. The morphologies are, in general, in good agreement with the flux distribution of the stellar component, showing no noticeable biconical outflow features (Figure 4). For 12 out of 20 AGNs, however, the [O III] flux distribution shows a lopsidedness from the stellar center of the host galaxy (Figure 5), although it is relatively uncertain due to the poor sampling ($0''.6$ spaxel in diameter, see Section 2) and the seeing size ($0''.7 - 1''.3$). In general, the spaxel with the maximum [O III] flux has an offset of ~ 1 spaxel from the center of the galaxy. Such a lopsidedness in the [O III] flux distribution is possibly due to the dust obscuration of either the approaching or receding component of biconical outflows (e.g., Crenshaw et al. 2010; Fischer et al. 2014; Bae & Woo 2014, 2016).

By performing the kinematic decomposition of [O III] as described in Section 3.1, we find that 15 out of 20 AGNs have a detectable broad component in the line profile. After separating the narrow and broad components from the line profile, we examine the morphologies of the [O III] flux distribution of the two components separately (middle and bottom panels in Figure 4, respectively). First, the spaxels with a broad component have a smaller extent than those with a narrow component. This is mainly due to difficulties in detecting a broad component from low S/N spectra at the outskirts of the FoV. Second, the spaxels containing the broad component show diverse morphologies. Among the 15 broad-component-detected AGNs, 8 AGNs show a compact, round-shape morphology, while the other 7 AGNs show an irregular (e.g., patchy or elongated) shape.

4.1.2. Kinematics

We present the kinematic properties of [O III] based on its total, narrow, and broad components. First, we examine the 2D maps of the line-of-sight velocity structure of the [O III]-emitting region (Figure 6). When we examine the total profile of [O III], we find that 18 AGNs show blueshifted (14)

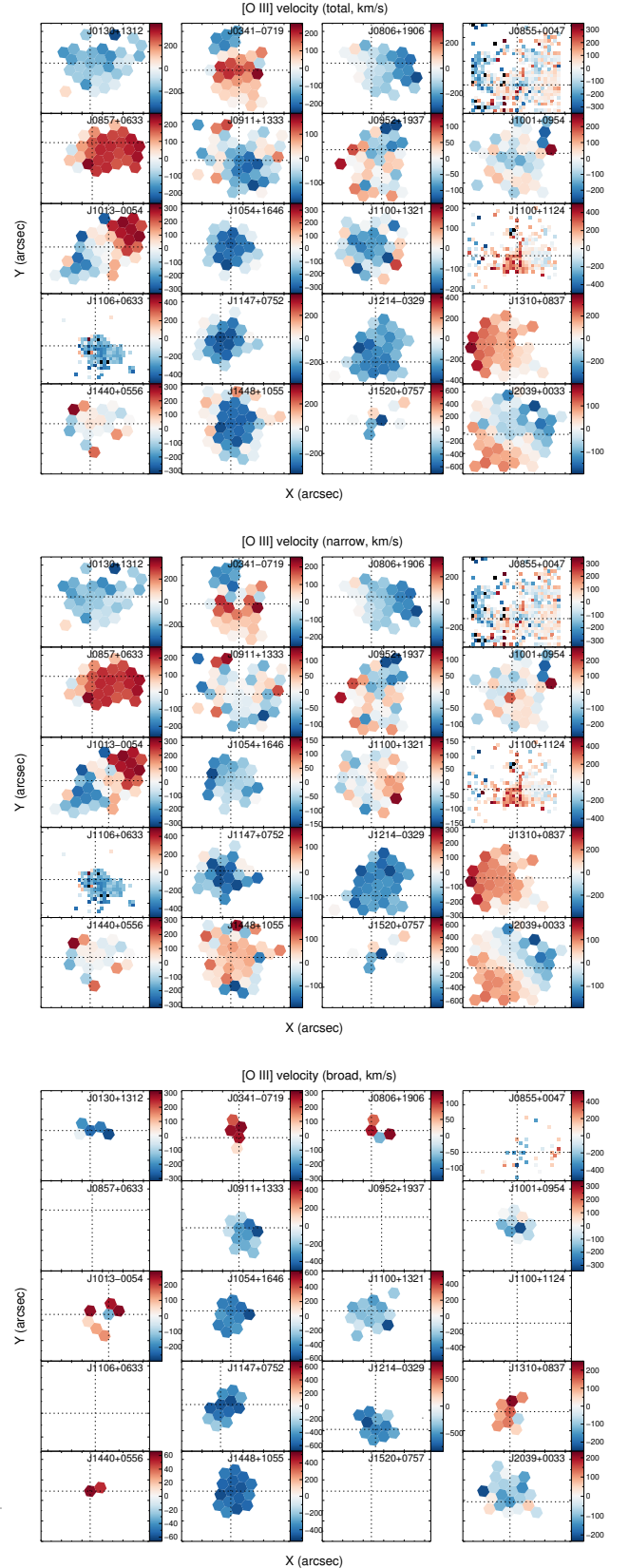


Figure 6. The [O III] velocity maps for the total (top panel), the narrow (middle panel), and the broad component (bottom panel). Blank maps indicate no detection of the AGNs. The major ticks in both x- and y-axes represent $1''$ for the Magellan targets, while the major ticks denote $5''$ for the VLT targets. The AGNs are listed in order of ascending R.A. from top-left to bottom-right.

Table 2
The characteristics of the spatially resolved velocity fields of the NLR

SDSS name (1)	[O III]			H α			Disk type (8)
	$V_{[\text{O III}],T}$ (2)	$V_{[\text{O III}],N}$ (3)	$V_{[\text{O III}],B}$ (4)	$V_{H\alpha,T}$ (5)	$V_{H\alpha,N}$ (6)	$V_{H\alpha,B}$ (7)	
J0130+1312	blue	blue	blue	rotation	rotation	rotation	SF
J0341-0719	red	rotation	red	rotation	rotation	rotation	SF
J0806+1906	blue	blue	red	rotation	rotation	rotation	AGN
J0855+0047	blue	blue	blue	blue	rotation	blue	SF
J0857+0633	red	red	–	rotation	rotation	–	AGN
J0911+1333	blue	blue	blue	blue	rotation	blue	SF
J0952+1937	blue	blue	–	rotation	rotation	blue	SF
J1001+0954	blue	rotation	blue	red	rotation	red	SF
J1013-0054	rotation	rotation	ambiguous	rotation	rotation	rotation	SF
J1054+1646	blue	blue	blue	blue	rotation	blue	AGN
J1100+1321	blue	rotation	blue	blue	rotation	blue	SF
J1100+1124	red	red	–	red	red	–	–
J1106+0633	blue	blue	–	blue	blue	blue	–
J1147+0752	blue	rotation	blue	blue	rotation	blue	SF
J1214-0329	blue	rotation	blue	blue	rotation	blue	SF
J1310+0837	red	red	red	rotation	rotation	–	AGN
J1440+0556	systemic	systemic	red	red	red	red	–
J1448+1055	blue	red	blue	blue	rotation	blue	AGN
J1520+0757	blue	blue	–	blue	blue	blue	–
J2039+0033	blue	rotation	blue	rotation	rotation	rotation	SF

Note. — (1) the name of AGN; (2) the characteristics of the velocity field based on the total profile of [O III]; (3) the same as (2) but based on the narrow component of [O III]; (4) the same as (2) but based on the broad component of [O III]; (5) the same as (2) but for the total profile of H α ; (6) the same as (2) but based on the narrow component of H α ; (7) the same as (2) but based on the broad component of H α ; (8) type of disk seen in the narrow component of H α .

or redshifted (4) velocity shifts within the central kpc or a more extended region, compared to the systemic velocity of the host galaxy. One AGN (J1013-0054) shows a rotational kinematics, and another AGN (J1440+0556) shows no or little velocity offset beyond the uncertainty in velocity offset measurement within the central kpc region.

When we focus on the broad and narrow components separately, the velocity structure looks different from the total component. The majority (10 out of 15) of broad-component-detected AGNs show negative velocity offset, while four AGNs show positive velocity offset and one AGN shows ambiguous velocity structure. The result is consistent with the model predictions of biconical outflows and dust obscuration, which expect a larger number of AGNs with negative velocity offset than those with positive velocity offset (Bae & Woo 2016). For the 15 broad-component-detected AGNs, the spaxels with a narrow component show mostly either negative velocity offset (5), positive velocity offset (2), rotational features (7), or no/little velocity offset (1) after removing the broad component (see Table 2).

Second, we examine the 2D maps of velocity dispersion of [O III] (Figure 7). The maps of total [O III] profile provide a hint for the mixture of narrow and broad component in the FoV. The range of velocity dispersion in the central region is from $\sim 200 \text{ km s}^{-1}$ to $\sim 600 \text{ km s}^{-1}$, which is much larger than the stellar velocity dispersions of the host galaxy. As we separate the broad and narrow components, the velocity dispersion of the broad component becomes larger up to $\sim 800 \text{ km s}^{-1}$, while that of the narrow component is, in general, broadly consistent with the stellar velocity dispersion. In the maps of the narrow component, we also find spaxels with a relatively large velocity dispersion at the boundary of spaxels with a broad component, which is possibly due to an un-removed broad component in the line profile.

Third, we investigate the radial distribution of the [O III] velocity and velocity dispersion for each component (Figure 8). In most cases, the absolute velocities of the broad components tend to become smaller as a function of distance from

the center, while those of the narrow components show a flat distribution as a function of distance. The velocity dispersions of the broad component are at least a few times larger than the stellar velocity dispersion, and also decreasing as a function of distance. In J0911+1333, for example, the velocity dispersions of the broad component are a factor of 4–6 larger than the stellar velocity dispersion. Such large velocity dispersions indicate non-gravitational origin, i.e., AGN outflows. In comparison, the velocity dispersions of the narrow component are larger than the stellar velocity dispersion by a factor of ~ 2 at the center, and become comparable to the stellar velocity dispersion at larger distance. We find that the trends in velocity dispersion of narrow and broad components are qualitatively similar for all 15 broad-component-detected AGNs.

Last, we compare the [O III] velocity and velocity dispersion for each component (Figure 9). We clearly see that the narrow and broad components are located in a different locus on the velocity-velocity dispersion (VVD) diagram. For example, J0911+1333 shows narrow components (blue dots) with larger velocity offsets compared to the broad components (red dot), while the velocities obtained from the total profile show a velocity in the middle of the velocities for narrow and broad component. The narrow components are located within 300 km s^{-1} of the velocity offset, while the broad components show a blueshifted velocity offset from -500 km s^{-1} to -100 km s^{-1} . The mean velocity dispersion of the narrow component is $\sim 200 \text{ km s}^{-1}$, while that of the broad component is $\sim 550 \text{ km s}^{-1}$. The rotational features and smaller range of velocity dispersion indicate that the narrow-component kinematics are related to the gravitational potential of the host galaxy, while the broad-component kinematics are due to non-gravitational phenomena.

4.2. the H α -emitting region

4.2.1. Morphology

We perform a visual inspection of the morphology of the H α flux distribution (Figure 10). Similarly to [O III], the morphology of the H α flux distribution follows the flux distri-

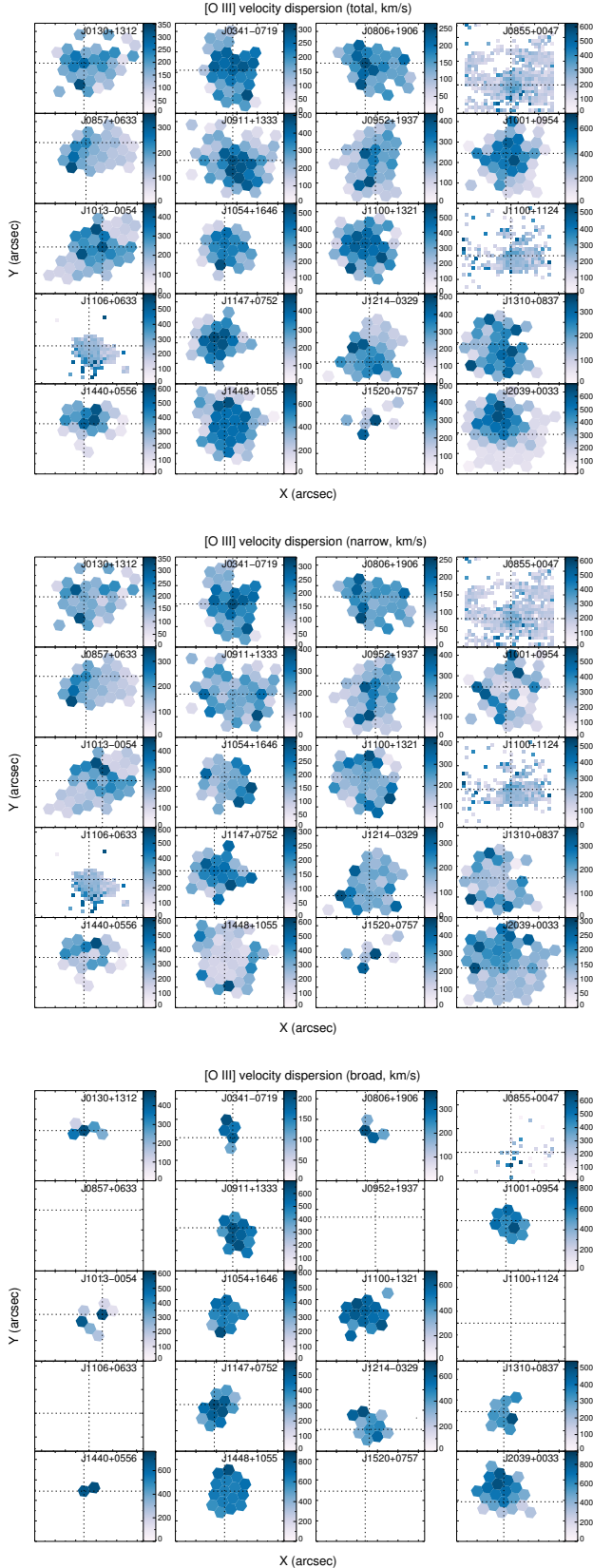


Figure 7. The [O III] velocity dispersion maps for the total (top panel), the narrow (middle panel), and the broad component (bottom panel). Blank maps for the broad component indicate no detection of the AGNs. The major ticks in both x- and y-axes represent $1''$ for the Magellan targets, while the major ticks denote $5''$ for the VLT targets. The AGNs are listed in order of ascending R.A from top-left to bottom-right.

bution of the stellar component in the host galaxy. We also find a lopsidedness in $H\alpha$ flux in six out of 20 AGNs (Figure 11). Interestingly, such asymmetry is more frequently found in [O III] (12 out of 20) than in $H\alpha$. All objects with $H\alpha$ flux lopsidedness also show [O III] flux lopsidedness, implying that what causes the lopsidedness in the flux distribution is commonly affecting both $H\alpha$ - and [O III]-emitting regions, but is less significant in $H\alpha$.

By performing a multi-Gaussian decomposition for the $H\alpha$ + [N II] lines, we find that 19 out of 20 AGNs have a detectable broad component in the $H\alpha$ line profile (bottom panel of Figure 10). Similarly to [O III], the spatial distribution of the broad $H\alpha$ component is smaller than that of the narrow component. Also, the morphologies of the spaxels with an $H\alpha$ broad component is mostly irregular, but somewhat comparable to those of the [O III] broad component. We find that all AGNs with a [O III] broad component (15) also have a broad component in $H\alpha$, implying a common physical origin for both broad components in [O III] and $H\alpha$. Also, there are four AGNs having a broad component in $H\alpha$ but not in [O III]. Among them, three AGNs have a lower S/N in [O III] than in $H\alpha$ while the remaining AGN (J1106+0633) has comparable S/N in [O III] and $H\alpha$. For this object, it is possible that the [O III] broad component was not revealed by our VLT/VIMOS observations, since the configuration has a low spectral resolution ($R \sim 720$).

4.2.2. Kinematics

We examine the velocity structure of the $H\alpha$ -emitting region (Figure 12). When we focus on the total component of $H\alpha$, we find that 13 AGNs show either negative (9) or positive (4) velocity offset, while the other seven AGNs show velocity structures similar to those of the stellar component, i.e., rotational or systemic velocity. If we examine the narrow component of $H\alpha$, we find that the velocity of the narrow $H\alpha$ is consistent with systemic or rotational velocity in most objects (16/20). Among the remaining four AGNs, two AGNs show negative velocity offset and the other two AGNs show positive velocity offset. After removing the broad component in the total profile, the velocity map of the narrow component of $H\alpha$ has the signature of Keplerian disk rotation (see Table 2). Rotational disk features are found in the narrow component of $H\alpha$ of 16 AGNs in our sample. Seven AGNs have a rotational disk feature in the narrow component of both $H\alpha$ and [O III], which are consistent with one another.

Similarly to [O III], the maps of the velocity dispersion of the total $H\alpha$ show clear signs of the mixture of narrow and broad component in the central region (Figure 13). The large velocity dispersion and spatial concentration of the broad component in $H\alpha$ also support its non-gravitational origin. After removing the broad component, the narrow components are, in general, consistent with the stellar velocity dispersion of the host galaxy.

Also, the distributions of $H\alpha$ velocity and velocity dispersion as a function of distance are qualitatively similar to those of [O III] (Figure 14), while the scales of the $H\alpha$ velocity and velocity dispersion are generally smaller than those in [O III]. Similarly, the narrow and broad components are clearly separated in the VVD diagram, as we found in the [O III] (Figure 15)

4.3. Sizes of the NLR and gas outflows

The size of the NLR (R_{NLR}) is typically measured based on the flux distribution of the emission lines, without taking into

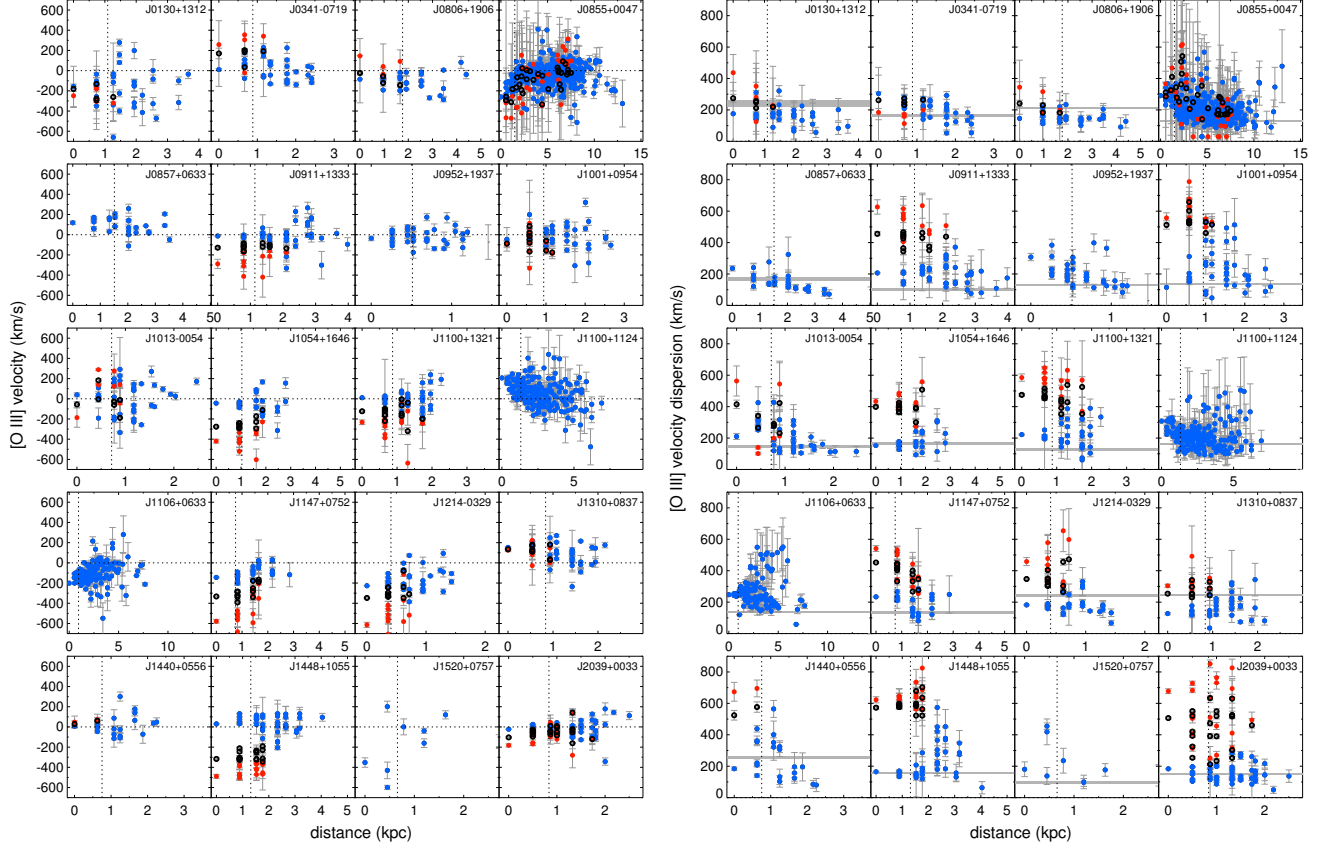


Figure 8. The radial distributions of the [O III] velocity (left) and velocity dispersion (right). Dotted lines in the vertical direction indicate the effective radius of the NLR based on [O III] (see Section 4.1). The dashed curves show the point-spread-function based on the seeing size. Each panel contains the radial distributions of the narrow component (blue), the broad component (red), if it exists, and the total (narrow+broad) component (black) with 1σ uncertainties. The gray shaded areas in the velocity dispersion panels indicate the range of stellar velocity dispersion from the SDSS with 1σ uncertainty. The AGNs are listed in order of ascending R.A. from top-left to bottom-right.

account of the outflow properties (e.g., Bennert et al. 2002; Schmitt et al. 2003; Liu et al. 2013a). To quantify the size of the outflows, we defined outflow size R_{out} , which is the radius where the [O III] velocity dispersion is equal to the stellar velocity dispersion of its host galaxy as Karouzos et al. (2016a). Here we use the two sizes, (R_{NLR}) and (R_{out}) to investigate the properties of the NLR and outflow kinematics, respectively.

First, we measure the flux-weighted mean size of the NLR (Husemann et al. 2014) for R_{NLR} as

$$R_{\text{NLR}} = \frac{\int R f(R) dR}{\int f(R) dR}, \quad (3)$$

where R is the distance from the center and $f(R)$ is the flux at a given distance. We only use the spaxels classified as composite or AGN from the emission-line diagnostics (e.g., Baldwin et al. 1981; Kauffmann & Heckman 2009). Then, we correct for seeing effects by subtracting the seeing size in quadrature, resulting in a $\sim 14\%$ decrease in size. Note that R_{NLR} for all targets is resolved compared to the seeing size. The mean R_{NLR} is $\sim 880 \pm 360$ pc for our sample with the mean $L_{[\text{O III}]}$ of $10^{40.7}$ erg s^{-1} , where $L_{[\text{O III}]}$ is extinction-uncorrected [O III] luminosity (see Table 3).

To estimate the uncertainty in R_{NLR} , we construct 100 mock spatial distributions of the [O III] region by randomizing the flux for each spaxel including noise, and we measure R_{NLR} in the same manner. Then we adopt 1σ of the distribution as

the uncertainty of R_{NLR} . In addition to this uncertainty, we add 10% of R_{NLR} to account for the uncertainty in the seeing size, and also add a half spaxel size (~ 0.3) to take into account the uncertainties from the spatial sampling. Note that R_{NLR} of J1100+1124 is regarded as the upper-limit of R_{NLR} since the target is observed using VLT/VIMOS, which has a large FoV, and the flux-weighted size includes some spaxels of spiral arms classified as composite region. These spaxels might be contaminated with shock-induced line emissions in the emission-line diagnostics.

Second, we measure the outflow size R_{out} based on the 1D distributions of the [O III] velocity dispersion as a function of distance from center (Figure 16). We obtain the mean value of the [O III] velocity dispersion from the spaxels as a function of distance, then determine the radius where the [O III] velocity dispersion is equal to the stellar velocity dispersion of the host galaxy, after linearly interpolating the mean values of the [O III] velocity dispersion (orange lines). We also correct the measured size by subtracting the seeing size in quadrature. We assume 20% of uncertainty in R_{out} . We obtain that the mean R_{out} is ~ 1800 pc, which is about a factor of two larger than the mean $R_{\text{NLR}} \sim 880$ pc (see Table 3). The result is in good agreement with the result from (Karouzos et al. 2016a), which reported that R_{out} is a few times larger than R_{NLR} . Four AGNs (i.e., J0130+1312, J0806+1906, J0857+0633, and J1310+0837), however, show smaller R_{out} than R_{NLR} due to

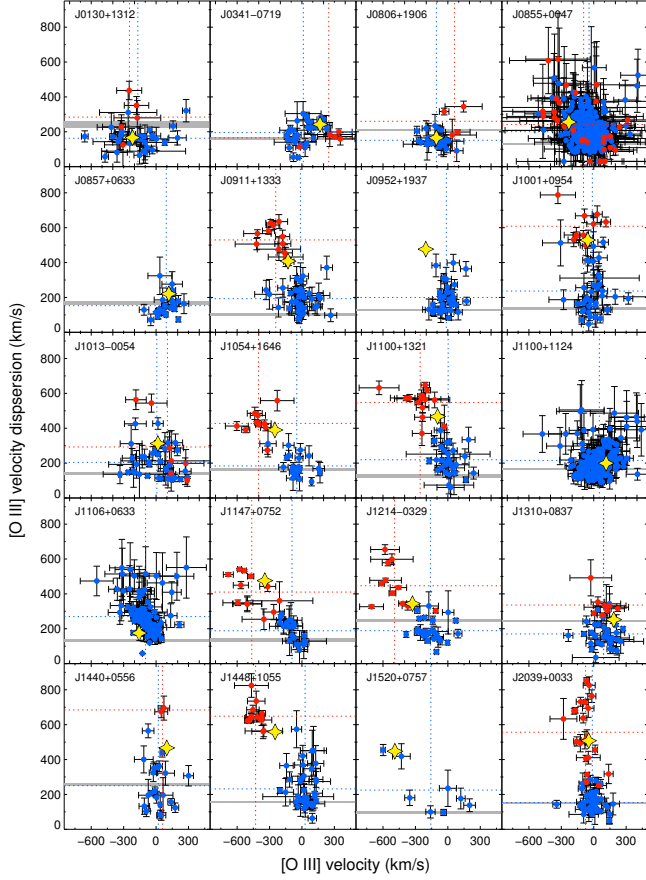


Figure 9. The velocity-velocity dispersion diagrams for the narrow (blue dots) and broad components (red dots) of the [O III] line. The error bars represent 1σ uncertainties in the measurement. Blue (red) dotted lines are the mean values of the velocity and velocity dispersion for the narrow (broad) component. Yellow stars are the values obtained from the SDSS spectra. The horizontal gray shaded areas indicate the range of stellar velocity dispersion from the SDSS with 1σ uncertainty. The AGNs are listed in order of ascending R.A from top-left to bottom-right.

their low [O III] velocity dispersion compared to the stellar velocity dispersion of the host galaxy, indicating that stellar velocity dispersion may not be the best parameter to separate the non-gravitational outflow signatures from the gravitation kinematics.

Based on our measurements of both R_{NLR} and [O III] luminosity, here we present the size–luminosity relationship (Figure 17). Since the relationships for type 1 and type 2 AGNs are in good agreement with one another (Schmitt et al. 2003), we also include 29 high-luminosity type 1 AGNs from the literature with mean $L_{[\text{O III}]}$ = $10^{42.4}$ erg s $^{-1}$ (Husemann et al. 2013, 2014) in which the R_{NLR} was measured in a consistent way with our study. We also include six type 2 AGNs obtained from the Gemini/GMOS-IFU (Karouzos et al. 2016a,b). For this comparison, we use the extinction-uncorrected [O III] luminosity and apply the cosmological parameters used in the work of Husemann et al. (2014), i.e., $\Omega_{\Lambda} = 0.70$, and $\Omega_m = 0.30$. We assume 10% uncertainty in $L_{[\text{O III}]}$. To fit the size–luminosity relation, we apply a forward regression method using the FITEXY code in the IDL library (e.g., Park et al. 2012), obtaining:

$$\log R_{\text{NLR}} = (0.41 \pm 0.02) \times \log L_{[\text{O III}]} - (14.00 \pm 0.77). \quad (4)$$

The slope $\sim 0.41 \pm 0.02$ is consistent with the slope reported by

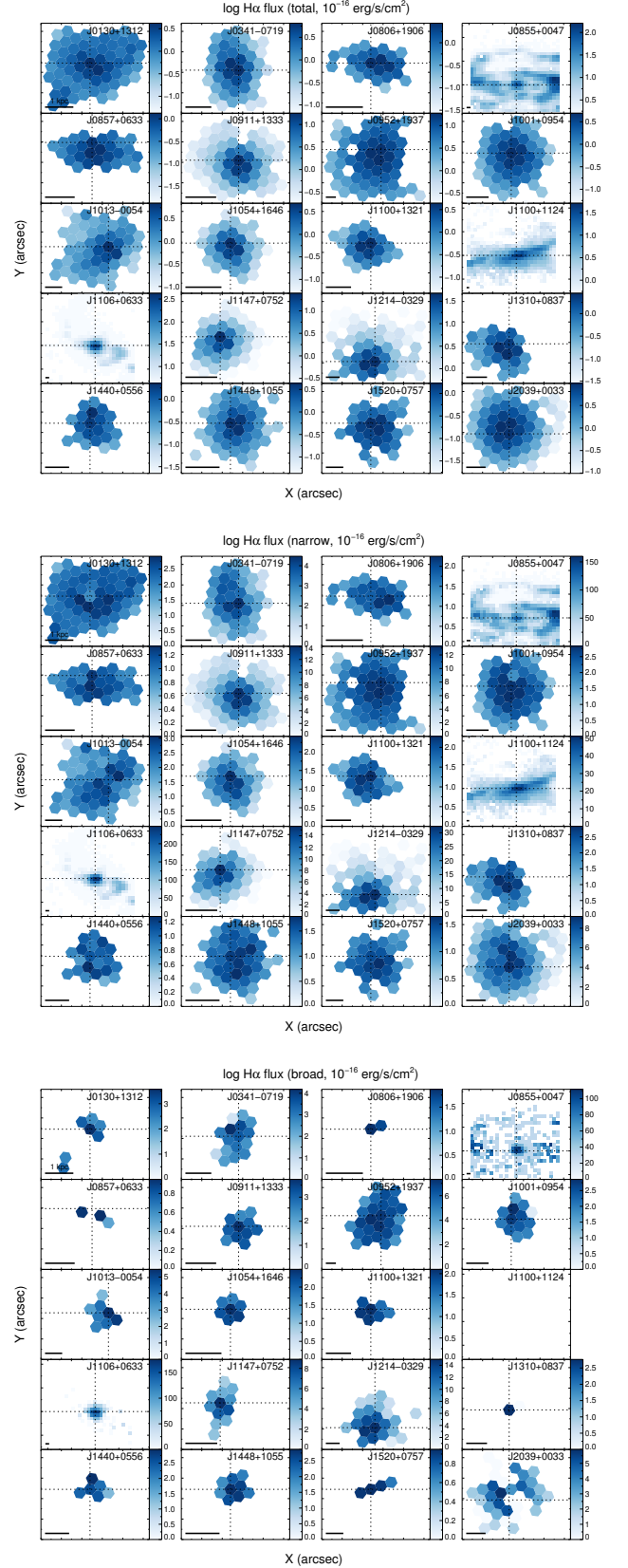


Figure 10. The flux maps (same as Figure 4) for H α .

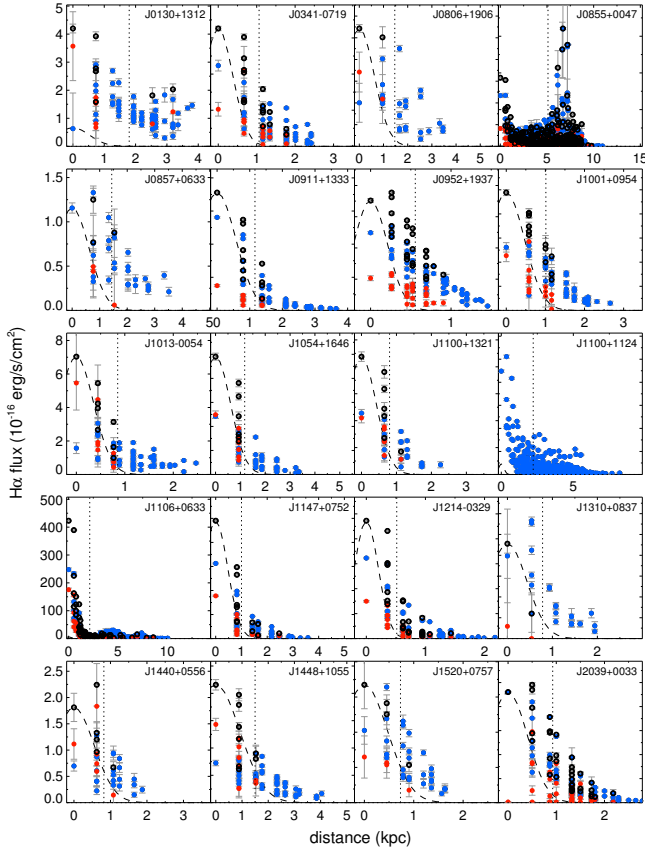


Figure 11. The radial flux distributions (same as Figure 5) for $H\alpha$.

Table 3
 $L_{[O III]}$ and the sizes of the NLR and outflows of the type 2 AGNs

SDSS name (1)	$\log L_{[O III]}$ (2)	$\log R_{NLR}$ (3)	$\log R_{out}$ (4)
J0130+1312	40.63	2.98 ± 0.20	2.37^a
J0341-0719	40.66	2.90 ± 0.21	3.14 ± 0.08
J0806+1906	40.91	3.22 ± 0.15	2.60^a
J0855+0047	40.41	3.16 ± 0.16	3.75 ± 0.08
J0857+0633	40.35	3.14 ± 0.14	2.69 ± 0.08
J0911+1333	41.01	2.99 ± 0.21	3.48 ± 0.08
J0952+1937	40.05	2.67 ± 0.15	3.01 ± 0.08
J1001+0954	40.79	2.91 ± 0.18	3.33 ± 0.08
J1013-0054	40.54	2.79 ± 0.18	2.82 ± 0.08
J1054+1646	41.06	2.93 ± 0.28	3.44 ± 0.08
J1100+1321	40.91	2.88 ± 0.22	3.28 ± 0.08
J1100+1124	39.55	3.11^a	3.37 ± 0.08
J1106+0633	40.77	2.96 ± 0.17	3.73^a
J1147+0752	41.28	2.77 ± 0.35	3.33 ± 0.08
J1214-0329	40.76	2.55 ± 0.25	2.80 ± 0.08
J1310+0837	40.89	2.86 ± 0.19	2.64 ± 0.08
J1440+0556	40.59	2.71 ± 0.31	3.02 ± 0.08
J1448+1055	41.31	2.97 ± 0.24	3.46 ± 0.08
J1520+0757	39.75	2.66 ± 0.25	3.04 ± 0.08
J2039+0033	40.90	2.86 ± 0.18	2.87 ± 0.08

Note. — (1) Name of the AGN; (2) extinction-corrected $[O III]$ luminosity in logarithm with uncertainty (erg s^{-1}); (3) the flux-weighted size of the NLR in logarithm with uncertainty (pc); (4) the kinematic size of outflows in logarithm with uncertainty (pc). Note that we adopt a different cosmology for the sizes and luminosity calculation as $H_0 = 70 \text{ km s}^{-1} \text{ Mpc}^{-1}$, $\Omega_\Lambda = 0.70$, and $\Omega_m = 0.30$, in order to have a consistency with the results in the literature.

^aUpper-limit of the sizes

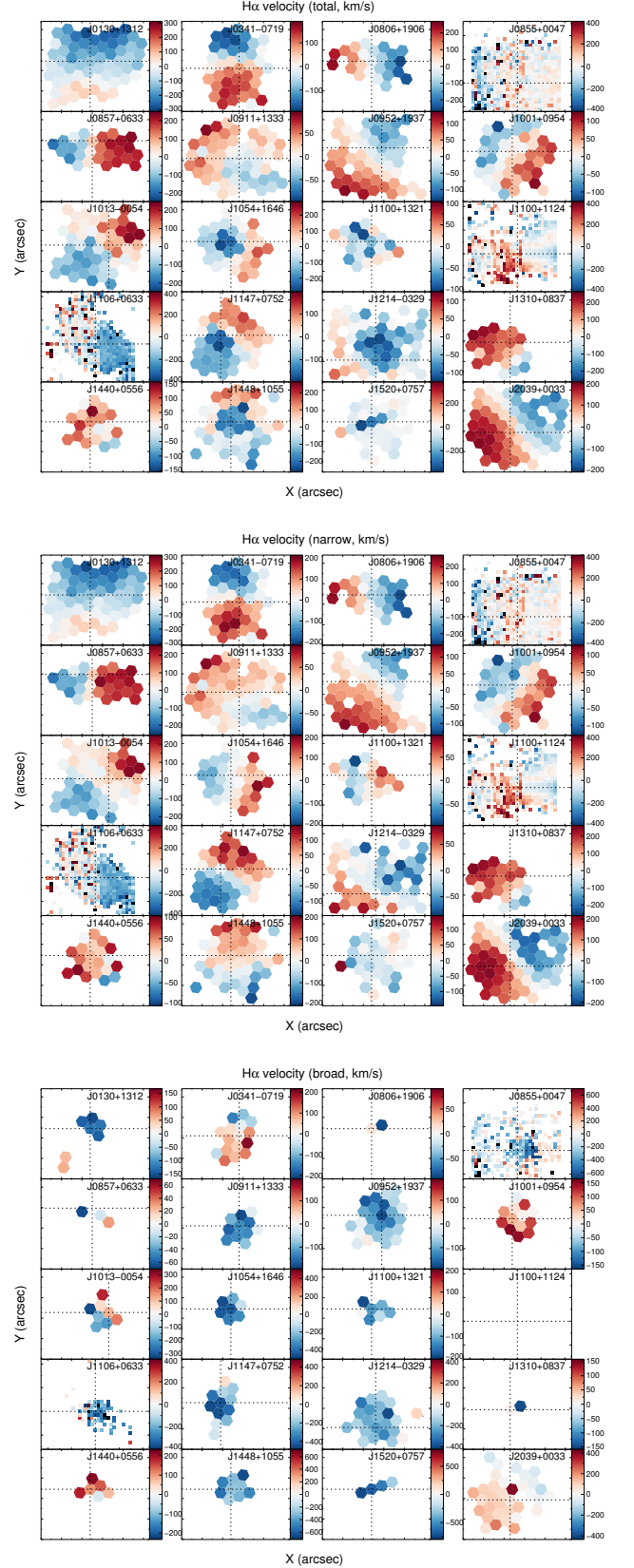


Figure 12. The velocity maps (same as Figure 6) for $H\alpha$.

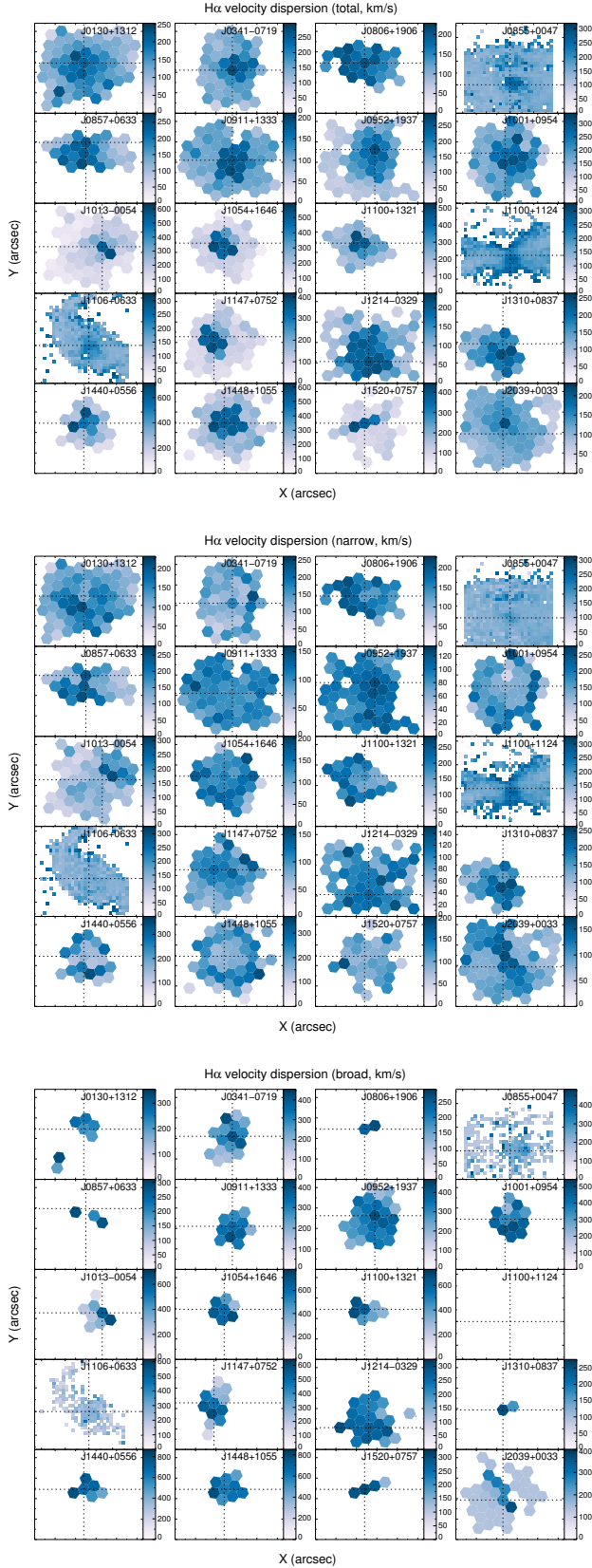


Figure 13. The velocity dispersion maps (same as Figure 7) for $H\alpha$.

Husemann et al. (2014) (0.44 ± 0.06).

The size–luminosity relation has been reported with different slopes based on different samples and methods, resulting in various physical interpretations for the relation. For example, Schmitt et al. (2003) found a slope of 0.33 ± 0.04 for local type 1 and 2 Seyfert galaxies by measuring the size and estimating the [O III] luminosity from the HST narrow-band imaging data. In addition, Liu et al. (2013a) found a slope of 0.25 ± 0.02 for type 2 quasars and Seyfert galaxies based on heterogeneous data from IFU and long-slit observations. To explain the physical conditions in the NLR of the sources, they argued that the pressure inside of NLR clouds (P) as well as the gas density (n) drops as radius r increases, i.e., $P(r) \propto r^{-2}$ and $n(r) \propto r^{-2}$, resulting in an ionization parameter (U) independent of radius. In contrast, other studies reported a slope of ~ 0.5 (Bennert et al. 2002; Husemann et al. 2014; Hainline et al. 2013). For example, Bennert et al. (2002) found a slope of 0.52 ± 0.06 for luminous Seyferts and quasars based on HST narrow-band imaging data. Similarly, Hainline et al. (2013) reported a slope of 0.4–0.5 for type 2 quasars and Seyfert galaxies, but they used the luminosity at $8\mu\text{m}$ as a proxy of AGNs luminosity rather than [O III] luminosity, arguing that the AGN luminosity is more directly traced by the luminosity of $8\mu\text{m}$ than of [O III]. To explain the slope of ~ 0.5 , these studies adopted a simple model that assumes a constant ionization parameter and the density for the clouds, which is not the case for our sample (see Section 5.1).

Similar to the photoionization size (R_{NLR})–luminosity relation, we examine the relationship between R_{out} and [O III] luminosity (Figure 18). Although the dynamic range of [O III] luminosity is rather small in our sample, we find no clear relationship between R_{out} and [O III] luminosity, presumably due to the dynamical timescale of the outflows. If we consider the relatively low outflow velocity $\sim 1000 \text{ km s}^{-1}$ and $R_{\text{out}} \sim 1\text{--}2 \text{ kpc}$, it will take $(1\text{--}2) \times 10^6$ years to reach R_{out} for the outflow, which is much larger than the photoionization timescale for the NLR. As a result, R_{out} may not show a clear relationship with $L_{[\text{O III}]}$ while R_{NLR} does. To further constrain whether there is a positive relationship between R_{out} and [O III] luminosity, we may need to obtain R_{out} from higher luminosity type 2 AGNs.

4.4. Properties of $H\alpha$ disk

In previous sections, we find both gravitational and non-gravitational kinematics in the NLR, and the non-gravitational kinematics are closely related to rotation as we noticed from the velocity maps of the narrow component of $H\alpha$. The properties of rotational disks in the sample are worth investigating, since they might provide useful hints on AGN feedback and co-evolution.

By using the integrated spectra within R_{NLR} , we classify the disk represented by the narrow $H\alpha$ into two groups: 1) SF-type ($\log [\text{N II}]/H\alpha \geq 0$); 2) AGN-type ($\log [\text{N II}]/H\alpha < 0$). Eleven AGNs are classified as SF-type, five AGNs are classified as AGN-type, while four AGNs have no/ambiguous rotation in $H\alpha$ (summarized in Table 2). We use the line ratio of the narrow component of $H\alpha$ and [N II] for disk classification, since we clearly see the rotational feature in the narrow component in $H\alpha$ but not in [O III], which strongly represents non-gravitational kinematics.

For the two groups, we compare the $D_n(4000)$ and $H\delta_A$ indices of the central region of AGN ($3''$ in diameter). We obtained the indices from the MPA-JHU catalog of SDSS DR7

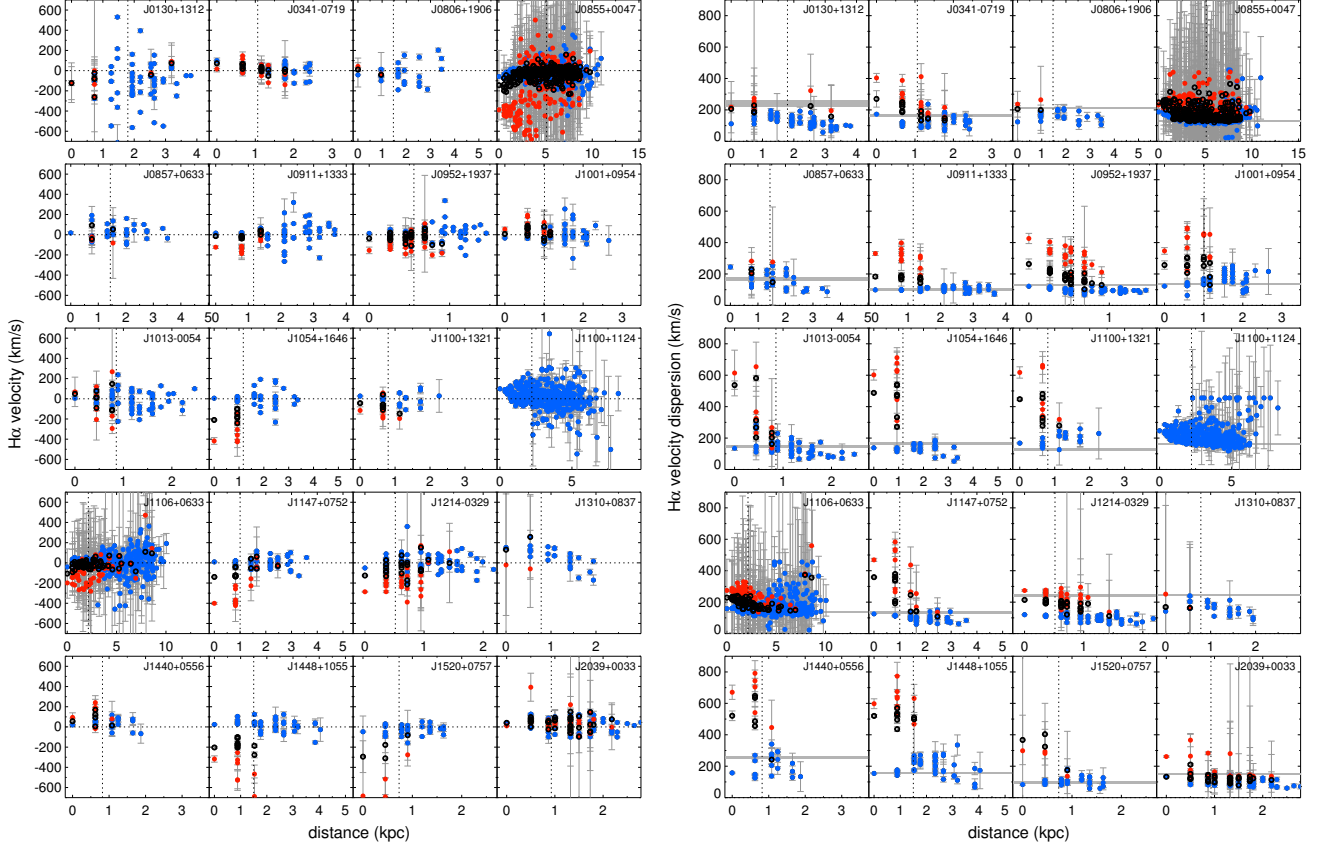


Figure 14. The radial distributions of velocity (left) and velocity dispersion (right) (same as Figure 8) for $H\alpha$.

galaxies. The two groups show clearly different ranges of indices. The SF-type group has $D_n(4000) = 1.37 \pm 0.13$ and $H\delta_A = 2.83 \pm 1.32$, while the AGN-type group has $D_n(4000) = 1.71 \pm 0.15$ and $H\delta_A = -0.08 \pm 0.92$, showing that the SF-type group has smaller $D_n(4000)$ and stronger $H\delta_A$ than the AGN-type group, as expected.

We also compare the distribution of specific star-formation rate (SSFR) as a function of the stellar mass (M_*) (Figure 19). We also adopted the SSFR and M_* from the MPA-JHU catalog of SDSS DR7 galaxies. The SSFRs for whole galaxy were estimated by combining the synthetic models on the integrated spectra and photometric information (Brinchmann et al. 2004), which provides SFRs sensitive over the past $10^8 - 10^9$ years (Kennicutt 1998). The AGNs with SF-type disks (blue dots) have higher SSFR ($\log \text{SSFR} = -10.0 \pm 0.4 \text{ yr}^{-1}$) and smaller stellar mass ($\log M_* = 10.6 \pm 0.3 M_\odot$), while the AGNs with AGN-type disks (red dots) have smaller SSFR ($\log \text{SSFR} = -11.3 \pm 0.7 \text{ yr}^{-1}$) and larger stellar mass ($\log M_* = 11.2 \pm 0.3 M_\odot$). The results consistently indicate that the AGNs with SF-type disks have on-going star formation at a similar level to that of star-forming galaxies of similar stellar mass (see Woo et al. 2017). We will compare the energetics of the AGNs with SF- and AGN-type disks and discuss the feedback scenario for the AGNs in Section 6.4.

5. ENERGETICS OF GAS OUTFLOWS

Measuring the physical properties of gas outflows (mass, energy, and momentum) is highly uncertain due to the complex nature of the NLR. However, a proper measurement of

those quantities is a crucial step towards understanding the co-evolution of galaxies and SMBHs. In the following, we describe the methods and results of estimates for the mass of ionized gas, energy, and momentum by using both spatially-resolved and integrated spectra. For simplicity, here we assume case B recombination and the biconical geometry for gas outflows (e.g., Crenshaw et al. 2010; Fischer et al. 2013; Bae & Woo 2016)

5.1. Spatially-resolved energetics

First, we calculate the energetics in each spaxel and examine the variation as a function of radial distance from the center. The ionized gas mass (M_{gas}) can be estimated as

$$M_{\text{gas}} = (9.73 \times 10^8 M_\odot) \times L_{H\alpha,43} \times n_{e,100}^{-1}, \quad (5)$$

where $L_{H\alpha,43}$ is the $H\alpha$ luminosity in units of $10^{43} \text{ erg s}^{-1}$, and $n_{e,100}$ is the electron density in units of 100 cm^{-3} (Nesvadba et al. 2006). We estimate n_e for each spaxel by using the [S II] line ratio (Osterbrock & Ferland 2006). Assuming a gas temperature of 10^4 K in the NLR, n_e in the central spaxel ranges from 54 to 854 cm^{-3} , with the mean value of $n_e \sim 360 \pm 230 \text{ cm}^{-3}$, which is consistent with previous studies (e.g., Nesvadba et al. 2006; Karouzos et al. 2016b). We find that both n_e and $L_{H\alpha}$ radially decrease with radial distance, thus M_{gas} also decreases outwards.

The kinetic energy of gas outflow (E_{out}) is the summation of bulk energy (E_{bulk}) and turbulence energy (E_{turb}) as

$$E_{\text{out}} = E_{\text{bulk}} + E_{\text{turb}} = \frac{1}{2} M_{\text{gas}} (v_{\text{gas}}^2 + \sigma_{\text{gas}}^2), \quad (6)$$

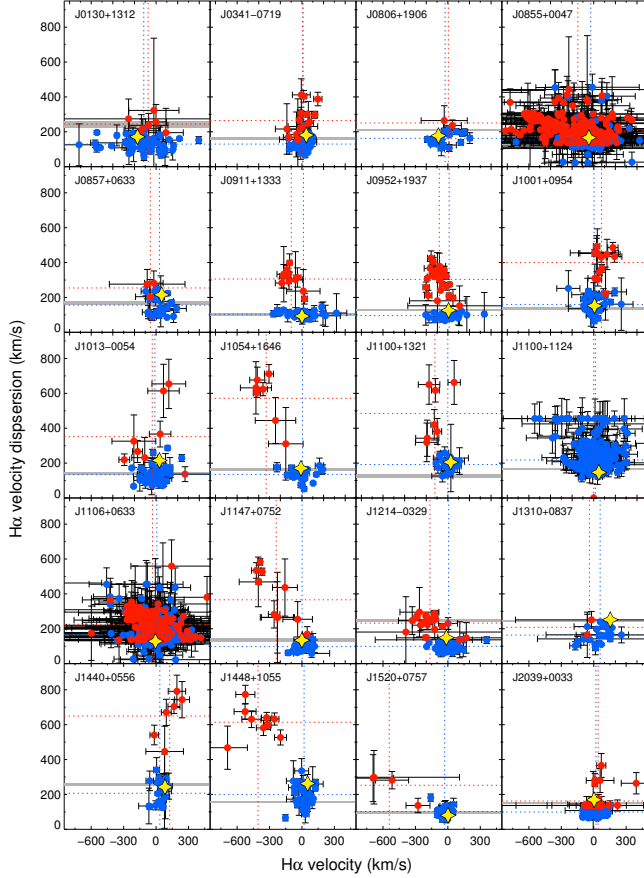


Figure 15. The VVD diagrams as the same with the Figure 9, but for $H\alpha$.

where M_{gas} is the estimated ionized gas mass, and v_{gas} and σ_{gas} are the velocity offset and the velocity dispersion measured from the total [O III] profile, respectively. The momentum (p) can be estimated as $p_{\text{out}} = M_{\text{gas}} v_{\text{gas}}$. For the estimation, we only use the spaxels where the [O III] and [S II]-doublet fluxes have $S/N > 3$. Since the [S II] line flux is in general weaker than the $H\alpha$ flux, the spatial extent of the estimation is mostly focused on the inner ~ 2 kpc of the AGNs, which is close to the size of R_{out} of the sample.

We find a general trend that the energy and momentum decrease ~ 1 order of magnitude per ~ 1 kpc increase in the radial distance in most of sample (Figure 20). Thus, we obtain distance-energy and distance-momentum relations by combining the energy and momentum per spaxel for the sample (Figure 21). We obtain the error-weighted values of energy and momentum at each bin of 0.5 kpc distance. By assuming the uncertainty of distance as a half of spaxel ($\sim 0.3''$), we also obtain the error-weighted values of distance at each bin. Then, we apply a forward regression method using the FITEXY code for the error-weighted values, obtaining:

$$\log E_{\text{out}} = (54.44 \pm 0.05) - (1.14 \pm 0.03) D_{\text{kpc}}, \quad (7)$$

$$\log p_{\text{out}} = (46.92 \pm 0.06) - (1.10 \pm 0.03) D_{\text{kpc}} \quad (8)$$

where D_{kpc} is the distance in units of kpc. The relationships show that both energy and momentum steeply decrease as a function of distance.

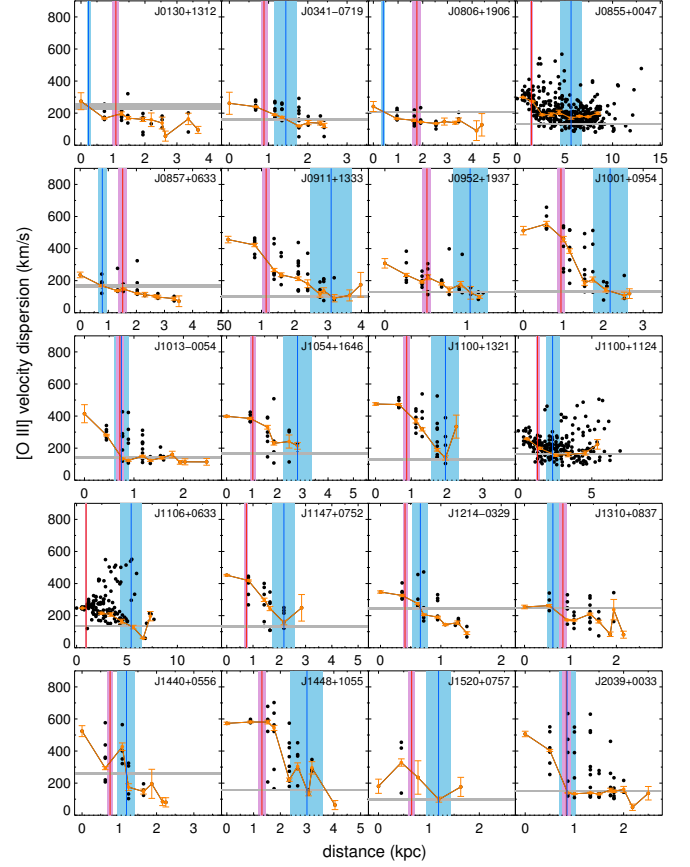


Figure 16. The radial distributions of the [O III] velocity dispersion (black dots) with the sizes of R_{NLR} and R_{out} (see Section 4.3). The velocity dispersions were measured from the total profile of [O III]. The calculated sizes of R_{NLR} and R_{out} are denoted with red and blue vertical lines, respectively. The shaded regions indicate the uncertainties of the sizes.

5.2. Integrated energetics: impact on the nuclear star-formation

As we determined two different sizes based on the flux distribution (R_{NLR}) and kinematics of the NLR (R_{out}), here we obtain the total energetics of the outflows (i.e., mass outflow rate, energy injection rate, and momentum flux) for the two different sizes and compare the results. We also compare the energetics of the groups of AGNs with different disk properties (Section 4.4) in order to investigate whether the nuclear star-formation is affected by AGN outflows.

5.2.1. Energetics for two different sizes

To estimate the total energetics of AGN outflows for two different sizes, we construct an integrated spectrum for both R_{NLR} and R_{out} of each AGN, then we calculate M_{gas} and n_e in the same manner as for the spatially resolved case. We also calculate the [O III] velocity offset and velocity dispersion from the integrated spectra. As we estimate the integrated energetics using two different sizes, we can directly compare the values and examine the effect of different sizes estimates on the energetics calculation.

If we assume biconical outflows with radius r and the ionized gas mass M_{gas} within r , the mass outflow rate \dot{M}_{out} can be calculated as

$$\dot{M}_{\text{out}} = \frac{M_{\text{gas}}}{\tau_{\text{dyn}}} = \frac{3M_{\text{gas}} v_{\text{out}}}{r}, \quad (9)$$

Table 4
Integrated physical properties of the type 2 AGNs within R_{NLR}

SDSS name (1)	$\log L_{[\text{O III}]}$ (2)	$\log L_{\text{bol}}$ (3)	\dot{M}_{acc} (4)	$v_{[\text{O III}]}$ (5)	$\sigma_{[\text{O III}]}$ (6)	σ_0 (7)	v_{out} (8)	$\log L_{\text{H}\alpha}$ (9)	n_e (10)	M_{gas} (11)	$\log E_{\text{kin}}$ (12)	\dot{M}_{out} (13)	$\log \dot{E}_{\text{out}}$ (14)	$\log \dot{p}_{\text{out}}$ (15)
J0130+1312	40.34	43.88	1.35	-175	193	260	520	40.54	370	9.2	54.40	1.5	41.12	33.70
J0341-0719	40.39	43.93	1.50	+144	246	285	570	40.58	122 ^a	30.3	54.99	6.6	41.83	34.38
J0806+1906	40.69	44.23	3.03	-86	187	205	411	40.72	344	14.8	54.39	1.1	40.78	33.47
J0855+0047	40.26	43.80	1.13	-230	285	366	732	40.41	171	14.6	54.89	2.3	41.59	34.02
J0857+0633	40.11	43.66	0.80	+122	177	215	430	40.24	129	13.1	54.38	1.2	40.86	33.53
J0911+1333	40.77	44.31	3.61	-132	429	449	898	41.19	583	26.2	55.32	7.3	42.27	34.62
J0952+1937	39.47	43.01	0.18	-63	345	351	702	40.49	78	38.5	55.28	17.7	42.44	34.89
J1001+0954	40.33	43.87	1.32	-25	548	548	1096	40.48	399	7.3	54.94	3.0	42.06	34.32
J1013-0054	40.11	43.65	0.80	+12	300	300	600	40.14	236	5.7	54.31	1.7	41.29	33.81
J1054+1646	40.72	44.27	3.27	-282	377	471	942	40.64	156	27.6	55.39	9.5	42.42	34.75
J1100+1321	40.56	44.10	2.24	-137	470	490	980	40.32	237	8.6	54.91	3.4	42.01	34.32
J1100+1124	39.53	43.07	0.21	+158	254	299	598	39.95	341 ^b	2.1	53.88	0.3	40.53	33.06
J1106+0633	40.46	44.00	1.78	-176	234	294	587	40.82	520	12.3	54.63	2.5	41.43	33.96
J1147+0752	40.65	44.19	2.73	-358	437	564	1129	40.64	327	12.8	55.21	7.6	42.48	34.73
J1214-0329	40.30	43.84	1.23	-281	331	434	869	40.70	761	6.4	54.69	4.9	42.06	34.43
J1310+0837	40.42	43.97	1.63	+172	250	304	608	40.09	321	3.7	54.13	1.0	41.05	33.56
J1440+0556	40.04	43.58	0.67	+42	480	482	964	39.96	854	1.0	53.98	0.6	41.24	33.56
J1448+1055	40.94	44.48	5.37	-293	576	646	1292	40.74	620	8.7	55.16	3.7	42.29	34.48
J1520+0757	39.16	42.70	0.09	-486	430	649	1297	39.77	54	10.6	55.25	9.2	42.69	34.88
J2039+0033	40.55	44.10	2.20	-71	468	474	947	40.71	251	19.8	55.25	7.8	42.35	34.67

Note. — (1) SDSS name of AGN; (2) Extinction-uncorrected [O III] luminosity in logarithm (erg s^{-1}); (3) AGN bolometric luminosity in logarithm as $L_{\text{bol}} = 3500 \times L_{[\text{O III}]}$ (erg s^{-1} , Heckman et al. 2004); (4) Mass accretion rate as $\dot{M}_{\text{acc}} = L_{\text{bol}}/\mu c^2$ ($10^{-2}M_{\odot} \text{ yr}^{-1}$); (5) [O III] velocity offset with respect to the systemic velocity of the stellar component (km s^{-1}); (6) [O III] velocity dispersion (km s^{-1}); (7) dust-corrected [O III] velocity dispersion (km s^{-1}); (8) bulk velocity of the outflows (km s^{-1}) (9) H α luminosity in logarithm (erg s^{-1}); (10) electron density estimated from the [S II] line ratio (cm^{-3}); (11) ionized gas mass in units of $10^5 M_{\odot}$ (see Equation 5); (12) kinetic energy in logarithm (erg); (13) mass outflow rate ($M_{\odot} \text{ yr}^{-1}$); (14) energy injection rate (erg s^{-1}); (15) momentum flux (dyne).

^aThe estimated electron density from the [S II] ratio is saturated to the lowest density allowed in the calculation (1 cm^{-3}). Hence we adopt the electron density from SDSS.

^bThe [S II]-doublet is affected by a telluric absorption band, so we adopt the electron density from SDSS.

Table 5
Integrated physical properties of the type 2 AGNs within R_{out}

SDSS name (1)	$\log L_{[\text{O III}]}$ (2)	$\log L_{\text{bol}}$ (3)	\dot{M}_{acc} (4)	$v_{[\text{O III}]}$ (5)	$\sigma_{[\text{O III}]}$ (6)	σ_0 (7)	v_{out} (8)	$\log L_{\text{H}\alpha}$ (9)	n_e (10)	M_{gas} (11)	$\log E_{\text{kin}}$ (12)	\dot{M}_{out} (13)	$\log \dot{E}_{\text{out}}$ (14)	$\log \dot{p}_{\text{out}}$ (15)
J0130+1312	38.82	42.36	0.04	-106	200	226	453	38.90	57	1.4	53.45	0.8	40.72	33.36
J0341-0719	40.53	44.07	2.09	+126	239	270	541	40.82	—	—	—	—	—	—
J0806+1906	39.80	43.34	0.39	-38	231	234	469	39.92	416	1.9	53.63	0.7	40.68	33.31
J0855+0047	40.42	43.96	1.63	-132	277	307	615	41.02	93	108.2	55.61	3.6	41.63	34.15
J0857+0633	39.73	43.27	0.33	+134	222	259	518	39.85	—	—	—	—	—	—
J0911+1333	40.99	44.54	6.10	-98	355	369	737	41.42	516	49.3	55.43	3.7	41.80	34.23
J0952+1937	39.64	43.18	0.27	-70	180	193	386	40.82	—	—	—	—	—	—
J1001+0954	40.63	44.17	2.62	-57	489	492	984	40.88	536	13.7	55.12	1.9	41.77	34.08
J1013-0054	40.14	43.69	0.86	-5	293	293	587	40.19	187	8.1	54.44	2.2	41.38	33.92
J1054+1646	41.00	44.54	6.18	-260	357	442	884	40.95	151	57.2	55.65	5.7	42.15	34.50
J1100+1321	40.82	44.37	4.09	-126	432	450	901	40.70	122	39.7	55.51	5.7	42.17	34.51
J1100+1124	39.64	43.19	0.27	+140	223	264	528	40.12	—	—	—	—	—	—
J1106+0633	40.64	44.19	271	-129	237	270	540	41.14	250	53.3	55.19	1.6	41.18	33.74
J1147+0752	41.17	44.71	9.07	-314	373	488	976	41.31	428	46.8	55.65	6.6	42.30	34.61
J1214-0329	40.49	44.03	1.89	-231	314	390	779	40.92	686	11.8	54.85	4.5	41.93	34.34
J1310+0837	40.25	43.79	1.09	+165	236	288	576	39.94	289	2.9	53.99	1.2	41.09	33.63
J1440+0556	40.25	43.79	1.09	+28	451	452	905	40.23	803	2.1	54.23	0.5	41.15	33.49
J1448+1055	41.22	44.76	10.22	-254	561	616	1232	41.10	729	16.7	55.40	2.2	42.02	34.23
J1520+0757	39.49	43.03	0.19	-505	466	687	1374	40.18	—	—	—	—	—	—
J2039+0033	40.53	44.07	2.08	-59	408	413	825	40.70	255	19.3	55.12	6.5	42.15	34.53

Note. — (1) SDSS name of AGN; (2) Extinction-uncorrected [O III] luminosity in logarithm (erg s^{-1}); (3) AGN bolometric luminosity in logarithm as $L_{\text{bol}} = 3500 \times L_{[\text{O III}]}$ (erg s^{-1} , Heckman et al. 2004); (4) Mass accretion rate as $\dot{M}_{\text{acc}} = L_{\text{bol}}/\mu c^2$ ($10^{-2}M_{\odot} \text{ yr}^{-1}$); (5) [O III] velocity offset with respect to the systemic velocity of the stellar component (km s^{-1}); (6) [O III] velocity dispersion (km s^{-1}); (7) dust-corrected [O III] velocity dispersion (km s^{-1}); (8) bulk velocity of the outflows (km s^{-1}) (9) H α luminosity in logarithm (erg s^{-1}); (10) electron density estimated from the [S II] line ratio (cm^{-3}); (11) ionized gas mass in units of $10^5 M_{\odot}$ (see Equation 5); (12) kinetic energy in logarithm (erg); (13) mass outflow rate ($M_{\odot} \text{ yr}^{-1}$); (14) energy injection rate (erg s^{-1}); (15) momentum flux (dyne).

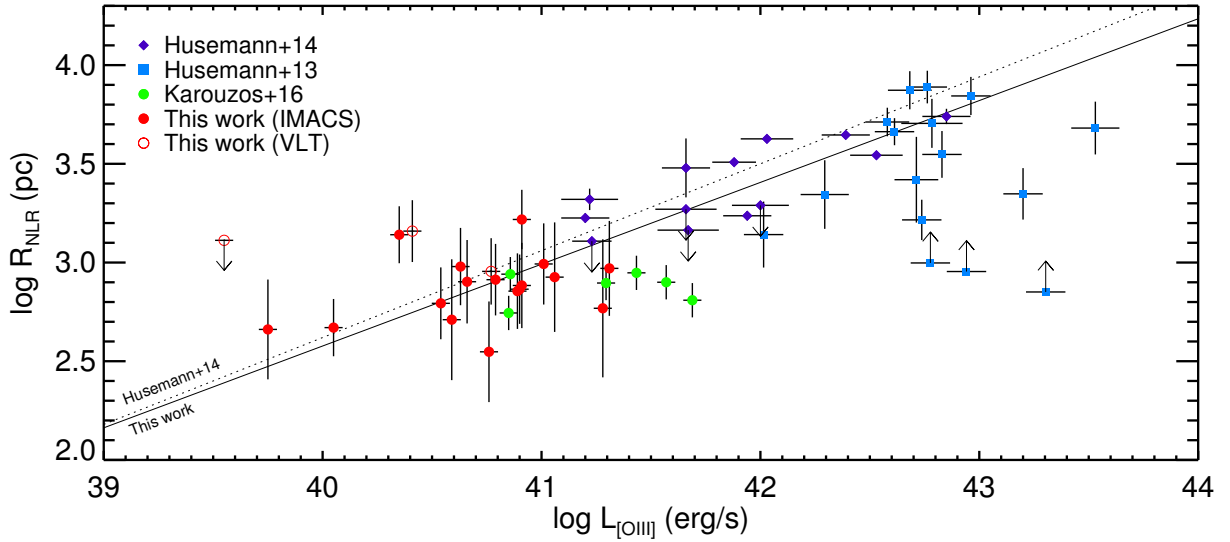


Figure 17. The size–luminosity relationship for R_{NLR} of 55 AGNs. We denote the 17 IMACS-observed AGNs with filled red dots and the 3 VIMOS-observed targets with unfilled red dots. To obtain the relationship for a larger dynamic range of [O III] luminosity, we compile the results from 29 luminous type 1 quasars at $z < 0.3$ (Husemann et al. 2013, 2014, blue squares and purple diamonds, respectively) and six type 2 AGNs (Karouzos et al. 2016a, green dots), in which R_{NLR} is measured in the same manner. The [O III] luminosity presented here is the extinction-uncorrected value. The solid line shows the slope of 0.41 resulting from our linear regression, while the other line indicates the slope from the literature as a comparison (Husemann et al. 2014).

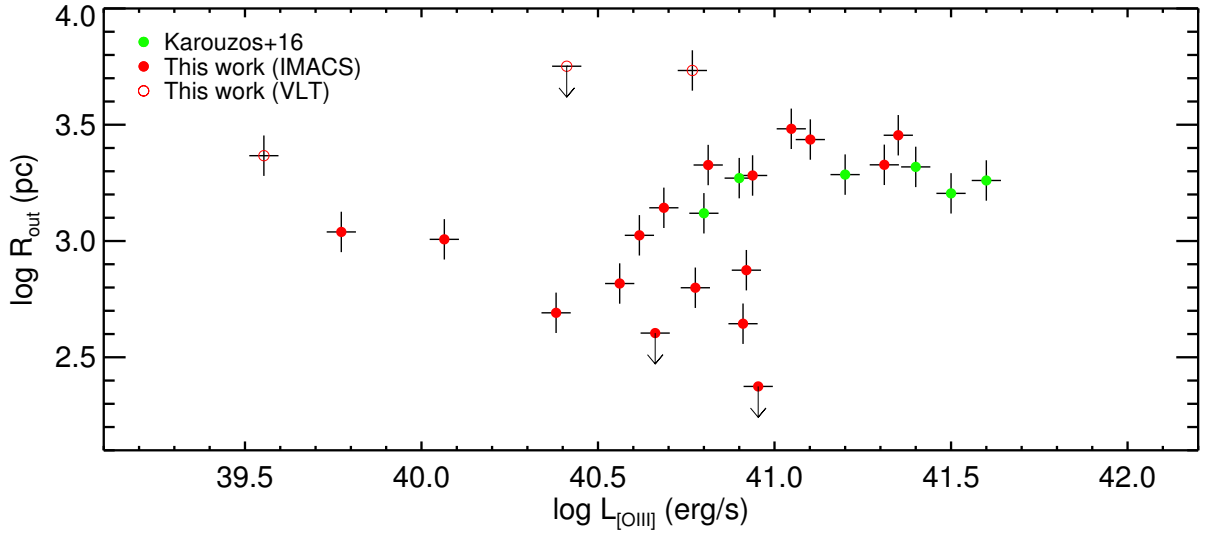


Figure 18. The size–luminosity relationship for R_{out} of 26 type 2 AGNs. We denote the 17 IMACS-observed AGNs with filled red dots, while the 3 VIMOS-observed targets with unfilled red dots. To obtain the relationship for a larger dynamic range of [O III] luminosity, we compile the results from six type 2 AGNs (Karouzos et al. 2016a, green dots), in which R_{out} is measured in the same manner. The [O III] luminosity presented here is the extinction-uncorrected value.

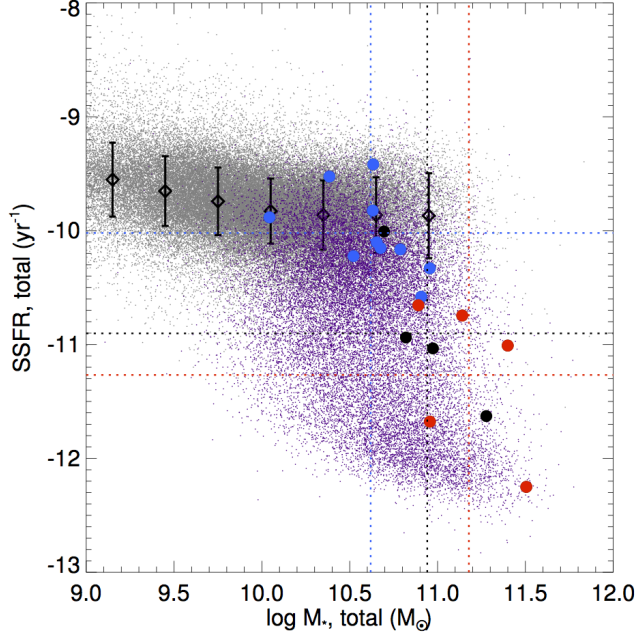


Figure 19. The distribution of specific star-formation rate (SSFR) and stellar mass for star-forming galaxies (gray) and AGN-host galaxies (purple). Blue, red, and black dots represent the different types of AGNs with SF-type disk, AGN-type disk, and no/ambiguous rotation, respectively. Black diamonds and error bars represent the mean values SSFR for star-forming galaxies at each bin of stellar mass and their 1σ distributions, respectively. Dotted lines represent the mean values of the stellar mass and specific star-formation rate for each group. (see Section 4.4).

where τ_{dyn} is the dynamical time for the ionized gas with v_{out} to reach a distance r , and v_{out} is the flux-weighted intrinsic outflow velocity, or bulk velocity of the outflows (Maiolino et al. 2012). Since we use the $H\alpha$ luminosity from the total profile of $H\alpha$ for our M_{gas} estimation (Equation 5), the results can be regarded as an upper limit of M_{gas} .

Then the energy injection rate \dot{E}_{out} and the momentum flux \dot{p}_{out} can be calculated as follows, respectively,

$$\dot{E}_{\text{out}} = \frac{1}{2} \dot{M}_{\text{out}} v_{\text{out}}^2, \quad (10)$$

$$\dot{p}_{\text{out}} = \dot{M}_{\text{gas}} v_{\text{out}}. \quad (11)$$

5.2.2. Estimation of the intrinsic outflow velocity

To calculate the energy injection rate and the momentum flux (Equations 9–11), we need to properly estimate the intrinsic outflow velocity v_{out} from the observations. We measured $\sigma_{[\text{O III}]}$ and $v_{[\text{O III}]}$, which are closely related to AGN outflows. However, these values are far from the intrinsic v_{out} , because the measured values were affected by dust extinction and projection effects, which can be more severe in type 2s than type 1s (e.g., Bae & Woo 2016). Hence, we need to assume proper outflow models to estimate v_{out} , which is difficult to estimate from observations.

For example, Liu et al. (2013b) assumed spherical symmetric or wide-angle biconical outflow models, resulting in the relationship of $v_{\text{out}} \sim 1.9 \times \sigma_{[\text{O III}]}$. This number may not be directly applicable to this study, however, since our sample consists less luminous than theirs, which may indicate a different outflow geometry (Bae & Woo 2016). Our sample are also type 2 AGNs, which can be more affected by projection

effects. To obtain the relationship of v_{out} and $\sigma_{[\text{O III}]}$ for our sample, hence, we exploit 3D biconical models suggested by Bae & Woo (2016), which successfully reproduced the distributions of the $[\text{O III}]$ kinematics of type 2 AGNs in SDSS (Woo et al. 2016).

In our models, we assume the exponentially decreasing radial flux profile $f(d) = A f_n e^{-\tau d}$, where f_n is the flux of the nucleus, and A is the amount of dust extinction ($0 < A < 1$) for each position in 3D. We adopt the range of $\tau=3-7$ and the size of the bicone as unity. We also assume different velocity profiles $v(d)$ (e.g., linear decrease or increase). Then, the intrinsic, flux-weighted v_{out} can be calculated as

$$v_{\text{out}} = \frac{\int f(d) v(d) dp}{\int f(d) dp}, \quad (12)$$

where p represents each position in 3D. The bicone has outer- and inner half-opening angles, and we use three different outer half-opening angles as 20° , 40° , and 60° . The inner half-opening angles are fixed as an half of the outer half-opening angle (Bae & Woo 2016). In calculations, we use the value of $\sigma_0 = (v_{[\text{O III}]}^2 + \sigma_{[\text{O III}]}^2)^{0.5}$ rather than $\sigma_{[\text{O III}]}$, because σ_0 can be a good proxy of the line width without dust extinction (Bae & Woo 2016).

By integrating the 3D bicone models, we calculate the intrinsic v_{out} and σ_0 as a function of bicone inclination (Figure 22). While v_{out} is a fixed value, σ_0 is minimized when the bicone axis is parallel to the plane of the sky ($i_{\text{bicone}}=0^\circ$) due to the projection effects. On the other hand, if the bicone is inclined to $\pm 40^\circ$, which is about the maximum inclination for type 2 AGNs (Marin 2014), σ_0 become larger due to lower projection effects. As a result, v_{out}/σ_0 has a large range from ~ 1.5 to ~ 2.5 if the outer half-opening angle of the bicone is 40° (middle panel).

For the IFU sample, we adopt a bicone half-opening angle of 40° , which is consistent with the mean value of half-opening angle estimated for 17 Seyfert galaxies based on HST/STIS data (Fischer et al. 2014). Hence, we adopt the relationship of $v_{\text{out}} = (2.0 \pm 0.5) \times \sigma_0$ in the energetics calculation for our sample. Alternatively, if the outer half-opening angle of the bicone is 20° (left panel) or 60° (right panel), v_{out}/σ_0 ranges from ~ 1.5 to ~ 4.5 and from ~ 1.5 to ~ 1.9 , respectively. Also, if we use different velocity profiles, the range of v_{out}/σ_0 becomes smaller than in the case of linear decrease.

5.2.3. Estimated energetics

First, we compare the ionized gas mass and outflow energetics obtained by using two different sizes (Figure 23). The estimated physical quantities within R_{NLR} and R_{out} are listed in Tables 4 and 5, respectively. Note that we could not measure the electron density for two AGNs (J0341–0719 and J1100+1124) when using R_{NLR} , and five AGNs (J0341–0719, J0857+0047, J0952+1937, J1100+1124, and J1520+0757) when using R_{out} . It is because the estimated electron densities based on $[\text{S II}]$ -line ratios are saturated to the lowest density (1 cm^{-3}) (J0341–0719, J0857+0047, J0952+1937, and J1520+0757), or the $[\text{S II}]$ -doublet is affected by the telluric absorption band (J1100+1124).

We find that the ionized gas mass using R_{out} is $\sim 2.3 \pm 1.9$ times larger than the mass using R_{NLR} (top-left panel), because R_{out} is a factor of ~ 2 larger than R_{NLR} (Section 4.3). However, the estimated energetics, i.e., outflow velocity (top-middle), total energy (top-right), mass outflow rate (bottom-left), energy injection rate (bottom-middle), and momentum

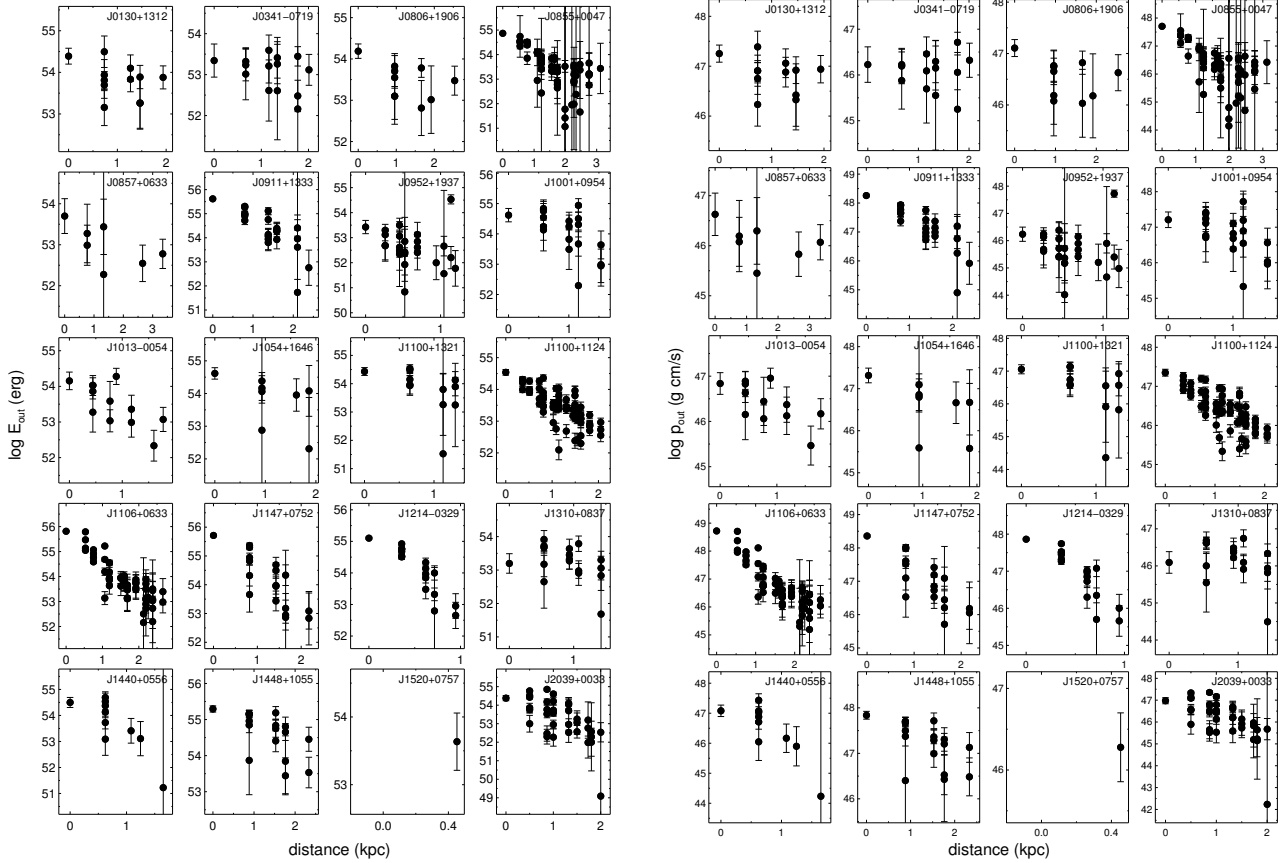


Figure 20. The energy (left) and momentum (right) distributions as a function of distance. The error bars denote 1σ uncertainties. The AGNs are listed in order of ascending R.A from top-left to bottom-right.

flux (bottom-right), are overall consistent with each other within uncertainties. The reason for this consistency is mainly due to relatively large uncertainties for the estimated quantities, e.g., outflow velocity and electron density. Also, the estimated outflow velocity does not change much when we increase the size since we estimate the velocity using the flux-weighted kinematics of [O III], which is exponentially decreasing from the nucleus. Hence, we will use R_{NLR} -based physical properties in the following analysis of the energetics of outflows. Note that we use the electron density from SDSS for two AGNs lacking this information from our data (J0341–0719 and J1100+1124).

The estimated M_{gas} is $(1.0\text{--}38.5)\times 10^5 M_{\odot}$ and the mass outflow rate \dot{M}_{out} is $0.3\text{--}17.7 M_{\odot} \text{ yr}^{-1}$. The mass accretion rate \dot{M}_{acc} can be calculated as $\dot{M}_{\text{acc}} = L_{\text{bol}}/\eta c^2$, where the η is the accretion efficiency typically assumed to be 0.1, and L_{bol} is the AGNs bolometric luminosity estimated as $L_{\text{bol}} = 3500 \times L_{[\text{O III}]}$, where $L_{[\text{O III}]}$ is the extinction-uncorrected [O III] luminosity (Heckman et al. 2004). The mean $\dot{M}_{\text{out}} \sim 4.6 \pm 4.3 M_{\odot} \text{ yr}^{-1}$ is consistent with the values of nearby AGNs ($0.1\text{--}10 M_{\odot}$, Veilleux et al. 2005). The estimated mean mass outflow rate is about a factor of ~ 260 higher than the estimated mean $\dot{M}_{\text{acc}} \sim 0.02 \pm 0.01 M_{\odot} \text{ yr}^{-1}$, indicating powerful mass loading of the AGN outflows by the ISM (e.g., Veilleux et al. 2005; Barbosa et al. 2009).

We also compare the energy injection rate and the momentum flux as a function of AGN bolometric luminosity (Figure 24). The estimated \dot{E}_{out} is $10^{40.5\text{--}42.7} \text{ erg s}^{-1}$ and the estimated \dot{p}_{out} is $10^{33.1\text{--}34.9} \text{ dyne}$. The majority of AGNs (18 out of

20) have relatively low energy injection rate, about $0.8 \pm 0.6\%$ of L_{bol} , and also have relatively low momentum flux, about $(5.4 \pm 3.6) \times L_{\text{bol}}/c$. Both the energy injection rate and the momentum flux for the AGNs are in general increasing as a function of L_{bol} . Interestingly, we find two AGNs (J0952+1937 and J1520+0757) with much higher energetics than the majority of AGNs in our sample. Although these two AGNs have relatively low bolometric luminosities ($L_{\text{bol}} \sim 10^{42.7\text{--}43.0} \text{ erg s}^{-1}$), their energy injection rate is 27–97% of L_{bol} and the momentum flux is 228–449 L_{bol}/c .

6. DISCUSSION

6.1. a mixture of the NLR kinematics: gravitational vs. non-gravitational

In Section 4.1 and 4.2, we investigate various properties, e.g., flux, velocity, and velocity dispersion, of [O III] and H α , respectively, in 1D and 2D, finding that the NLR is a mixture of non-gravitational, i.e., AGN outflows, and gravitational kinematic, i.e., rotation or random motion (see also Karouzos et al. 2016a). The non-gravitational kinematics are commonly detected in the broad component of both [O III] and H α , which are revealed by their large velocity dispersion compared to the stellar velocity dispersion and/or their large velocity offset with respect to the systemic velocity of the host galaxy. While the broad components of [O III] and H α show qualitatively similar non-gravitational kinematics, the absolute value of velocity and velocity dispersion of H α are relatively smaller than those of [O III].

We find a clear sign of gravitational kinematics (i.e., Keple-

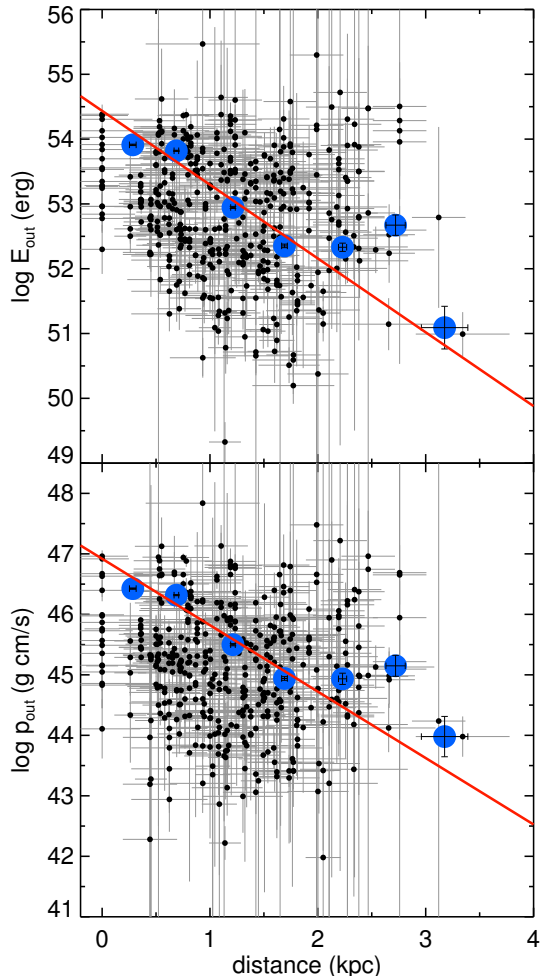


Figure 21. The combined energy (top) and momentum (bottom) distributions as a function of distance. Blue dots are the error-weighted values at each bin of 0.5 kpc distance, and the red lines are the result of linear regression for the error-weighted values. The error bars denote 1σ uncertainties.

rian rotation) in the narrow component of $H\alpha$ for most objects (16 out of 20 AGN). The other four AGNs, which do not show any rotation in the narrow component of $H\alpha$, may also have gravitational kinematics such as a random motion. In comparison, only 8 out of 20 AGNs show the gravitational kinematics (i.e., rotation or random motion) in the narrow component of [O III], implying that the gravitational kinematics are more significantly presented in $H\alpha$ than [O III]. Consider a simple picture that biconical outflows and a star-forming disk co-exist in the nucleus. Then, the star-forming disk is responsible for the gravitational kinematics, while the biconical outflows are responsible for the outflow kinematics in the NLR. In general, the star-forming region emits the stronger Balmer emission than the [O III] emission, so the rotational feature is more distinguishable in $H\alpha$ than in [O III]. For the same reason, the outflowing region, which is ionized by AGN, emits stronger [O III] than Balmer lines. Thus, the outflow kinematics are more noticeable in [O III] than in $H\alpha$.

In Section 4.4, we further focus on the origin of rotational features the relation of the narrow component of $H\alpha$ with star formation. We find that 11 AGNs with SF-type disks show lower $D_n(4000)$ and higher $H\delta$ indices than the AGNs with

AGN-type disks, showing that the AGNs with SF-type disks have on-going star formation, while five AGNs with AGN-type disks do not. The results further support that, even in the AGNs with strong outflows, the star-forming disk and AGN outflows co-exist in the nucleus (\sim central kpc), as several studies pointed out (e.g., Davies et al. 2016, Woo et al. 2017)

6.2. Driving mechanism of the outflows

While it is clear that the ionized gas outflows of our sample are mainly due to AGN activity (see Section 5.2), we further investigate the driving mechanism of the outflows. Theoretical studies expect that the outflows is energy conserving if the outflowing gas expand as a hot bubble without efficient cooling, while the outflow is momentum conserving if the outflows rapidly cool down and lose their energy (see King & Pounds 2015, for a review). AGN outflows would generate a different impact on the host galaxy depending whether the outflows are energy- or momentum conserving.

Since the driving mechanism depends on the properties of the accretion wind and the ISM of the host galaxy, it is still under debate which phase is dominant when and at what physical scales (e.g., Silk & Rees 1998; Faucher-Giguère & Quataert 2012; Zubovas & Nayakshin 2014). For example, King & Pounds (2015) imagine a scenario where the outflows are initially momentum conserving due to rapid cooling of the wind. In this case, the outflows lose their energy and can not remove the ISM, so the SMBH grows until it reaches the $M_{\text{BH}}-\sigma_*$ relation. When the SMBH has grown enough, the energy-conserving phase starts. This phase is more energetic than the momentum-conserving phase. As the energy-conserving outflows boost the momentum at larger scales, the outflows sweep the ISM and may suppress the growth of the SMBH. Faucher-Giguère & Quataert (2012) argue that the energy-conserving outflows are plausible if the wind is fast ($> \sim 10,000 \text{ km s}^{-1}$), or even if the wind is slow ($> \sim 1,000 \text{ km s}^{-1}$) with more restricted conditions.

Since the momentum flux compared to L_{Bol}/c of our sample are much larger than unity in most cases, we assume that the wind-driven outflows at the nucleus expand to large-scale (\sim kpc) outflows via the energy-conserving phase as

$$\dot{M}_{\text{gas}} v_{\text{gas}}^2 \approx f \dot{M}_{\text{in}} v_{\text{in}}^2, \quad (13)$$

where \dot{M}_{in} and v_{in} are the initial mass outflow rate and initial velocity in the nucleus, respectively. f is an energy transfer efficiency from small-scale wind to large-scale outflow. We adopt an efficiency of 0.2 based on recent observational results (Tombesi et al. 2015).

The momentum boost, i.e., $\dot{p}_{\text{gas}}/\dot{p}_{\text{in}}$, where $\dot{p}_{\text{gas}} = \dot{M}_{\text{gas}} v_{\text{gas}}$ and $\dot{p}_{\text{in}} = \dot{M}_{\text{in}} v_{\text{in}}$ can be calculated by combining with Equation 13 as follows

$$\frac{\dot{p}_{\text{gas}}}{\dot{p}_{\text{in}}} \approx 0.2 \frac{v_{\text{in}}}{v_{\text{gas}}}. \quad (14)$$

By using this equation, we estimate the values of v_{gas} and \dot{p}_{gas} with the expectations from the energy-conserving outflow by assuming $\dot{p}_{\text{in}} = L_{\text{bol}}/c$ (Figure 25). We find that most AGNs lie within $v_{\text{in}} = (0.01 - 0.3)c$, which is broadly consistent with ultra fast outflows (UFOs, $v_{\text{in}} \approx (0.1 - 0.4)c$) detected in X-ray observations (e.g., Tombesi et al. 2015). We do not find, however, any clear evidence for instantaneous quenching of the star formation due to outflows, since 11 out of 20 AGNs still show a sign of on-going star formation (see Sections 4.4 and 6.1).

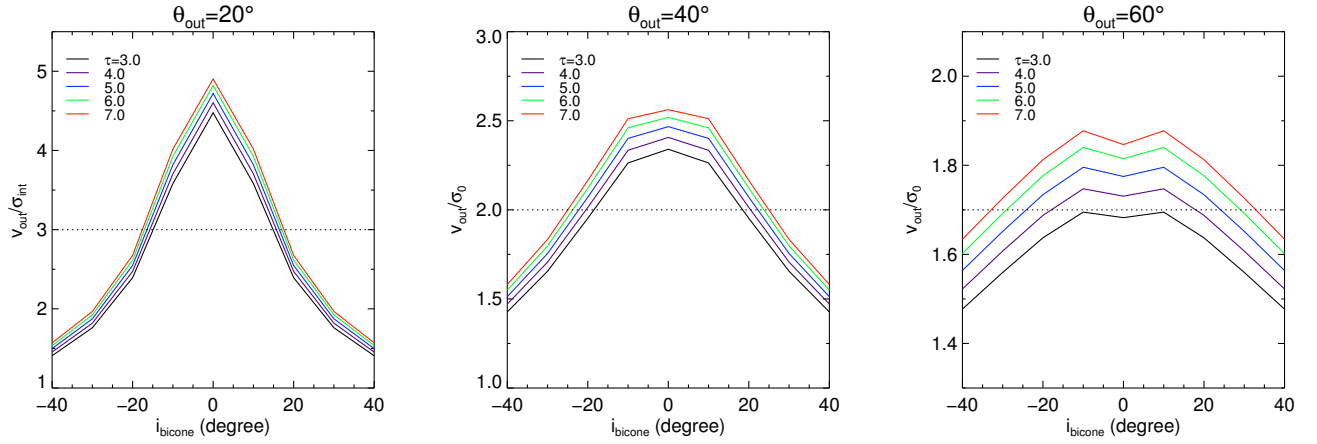


Figure 22. Distributions of v_{out}/σ_0 as a function of bicone inclination with a linearly decreasing velocity profile for bicone outer- and inner half-opening angle = $[40^\circ, 20^\circ]$ (left), $[40^\circ, 20^\circ]$ (middle), and $[60^\circ, 30^\circ]$ (right), respectively. Lines of different colors represent the different radial flux profiles of the bicone, i.e., $f(d) = f_n e^{-\tau d}$, where f_n is the flux of the nucleus.

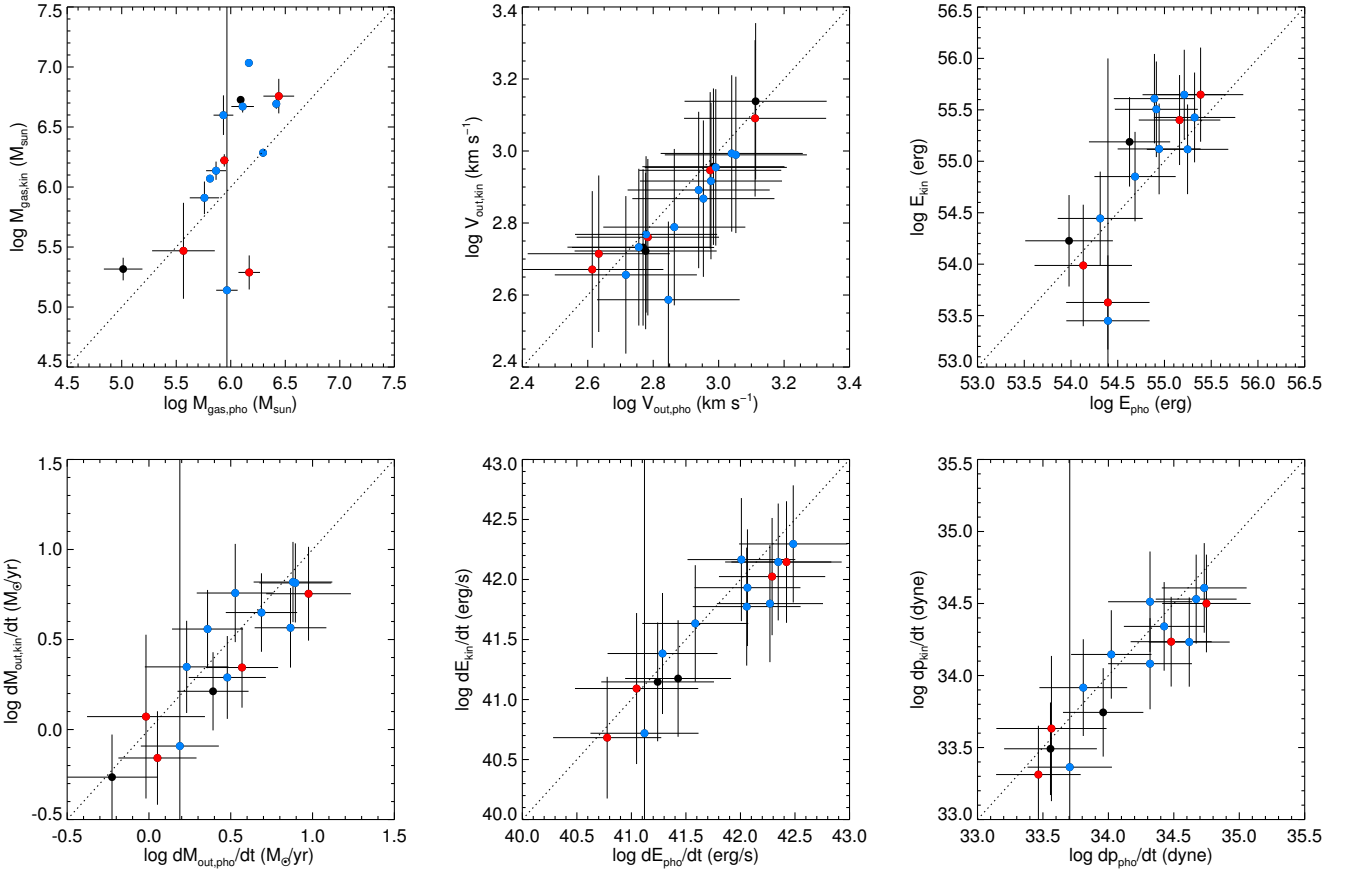


Figure 23. Comparisons of the integrated energetics when using two different sizes, i.e., flux-weighted NLR size (x-axis) and kinematics-based outflow size (y-axis): ionized gas mass (upper-left), intrinsic outflow velocity (upper-middle), total energy (upper-right), mass outflow rate (lower-left), energy injection rate (lower-middle), and momentum flux (lower-right). Blue, red, and black dots represent the different types of AGNs with SF-type disk, AGN-type disk, and no/ambiguous rotation, respectively. Error bars represent the 1σ uncertainties of the estimation.

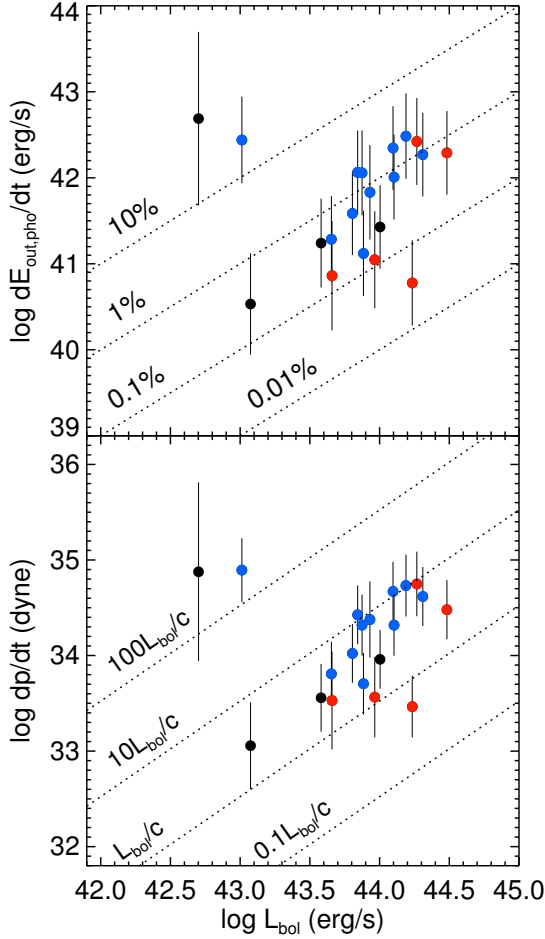


Figure 24. The energy injection rate (upper panel) and the momentum flux (lower panel) as a function of AGN bolometric luminosity for 20 AGNs. Blue, red, and black dots represent the different types of AGNs with SF-type disk, AGN-type disk, and no/ambiguous rotation, respectively. Error bars represent the 1σ uncertainties of the estimation.

On the contrary, if it were the momentum-conserving phase, the momentum boost would be expected to be 0.2 regardless of v_{gas} , which is not the case for our sample. These results imply that energy-conserving outflows due to accretion-disk wind might be the driving mechanism of the ionized gas outflows observed in the sample.

Note that we have two extreme AGNs with a high momentum boost (J0952+1937 and J1520+0757), which lead to unphysically large $v_{\text{in}} > c$, although the uncertainties are large. One possibility is that the f factor is larger for these AGNs due to largely different ISM composition. For J1520+0757, however, it is difficult to obtain $v_{\text{in}} < c$ even with $f = 1$. Another possibility is that the two AGNs may have much lower L_{bol} at present compared to the time when the outflow was launched, resulting in an overestimated momentum boost compared to the true value. We will discuss this scenario in the following section.

6.3. Time-delayed AGN outflows

In Sections 5.2 and 6.2, we find two AGNs with extreme energetics, while their bolometric luminosities are relatively low (J0952+1937 and J1520+0757). These two AGNs have the lowest electron density among the sample ($n_e=78$ and 54

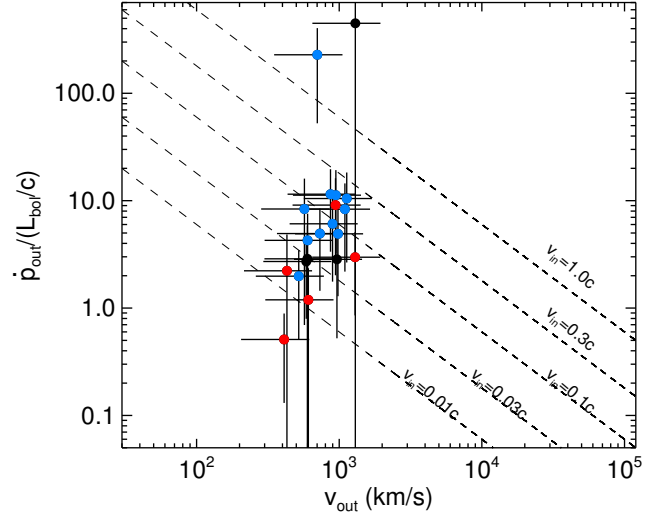


Figure 25. The momentum flux of gas outflows \dot{p}_{gas} normalized to L_{bol}/c as a function of the gas outflow velocity v_{gas} . Blue, red, and black dots represent the different types of AGNs with SF-type disk, AGN-type disk, and no/ambiguous rotation, respectively. Error bars represent the 1σ uncertainties of the estimation. Dashed lines indicate the initial velocity v_{in} of small-scale wind as $v_{\text{in}} = (0.01, 0.03, 0.1, 0.3, 1.0) \times c$ respectively from bottom-left to top-right, where c is the speed of light.

cm^{-3} , respectively), implying that the ionized gas has possibly been swept out, which is consistent with their high mass outflow rate ($\dot{M}_{\text{out}}=17.7$ and $9.2 M_{\odot} \text{ yr}^{-1}$, respectively). Then, what can cause the discrepancy between their energetics, e.g., energy injection rate and momentum flux, and the bolometric luminosity? Since we measured the bolometric luminosity of AGNs based on the [O III] luminosity in the NLR, the difference between the photoionization timescale ($\sim 10^4$ years) and the dynamical timescale of the outflows ($\sim 10^6$ years) to reach the NLR may cause the discrepancy. We note that this is the same explanation for the weak relationship between R_{out} and the [O III] luminosity (see Figure 18).

Let's consider the energy-conserving outflow expanding from high velocity, small-scale winds close to the nucleus (see Section 6.2). As the winds expand, the hot bubble would sweep out the surrounding ISM and the outflow velocity would become smaller. If we simply consider the constant outflow velocity of 1000 km s^{-1} , it will take 10^6 years, which is the dynamical timescale of outflows, to reach the ISM up to R_{out} of 1 kpc. Also, we find that the mean mass outflow rate is $\sim 4.6 M_{\odot} \text{ yr}^{-1}$ for the sample, so the ionized gas within R_{NLR} will be removed after $\sim 10^5$ years. Since the outflow would sweep out the ISM in the vicinity of the SMBH within a much shorter time scale $\ll 10^5$ years, it is possible that the AGN becomes inactive while the outflows propagate in the NLR ($\sim \text{kpc}$). Hence, the AGN can be inactive or less luminous when the powerful outflow reaches the NLR.

6.4. Do AGN outflows affect star formation?

From the integrated spectra within R_{NLR} , we estimate the physical properties related to the energetics of gas outflows, such as mass outflow rate, energy injection rate, and momentum flux (Section 5.2). We find the mean outflow velocity $v_{\text{out}} \sim 800 \text{ km s}^{-1}$ and the mean $R_{\text{NLR}} \sim 900 \text{ pc}$. The dynamical time t_d is given by $t_d = R_{\text{NLR}}/v_{\text{out}} \sim 10^6$ years, which is an order of magnitude smaller than the theoretical expect-

tation of 10^7 years for quasar lifetimes (e.g., Hopkins et al. 2006). The AGNs have a mass outflow rate $\dot{M}_{\text{out}} = 0.3\text{--}17.7 M_{\odot} \text{ yr}^{-1}$ with a mean value of $\sim 4.6 M_{\odot} \text{ yr}^{-1}$, which is a factor of ~ 300 larger than the mean mass accretion rate $\dot{M}_{\text{acc}} \sim 0.02 M_{\odot} \text{ yr}^{-1}$. For this mean gas mass for AGNs ($\sim 1.4 \times 10^6 M_{\odot}$) and mean mass outflow rate ($\sim 4.6 M_{\odot} \text{ yr}^{-1}$), it would take $\sim (4.2 \pm 3.1) \times 10^5$ years to remove the ionized gas from the $R_{\text{NLR}} \sim 1$ kpc, which is less than the dynamical timescale of AGNs $\sim 10^6$ years. Such gas removal timescale ($\sim 4.2 \times 10^5$ years) is comparable to the AGN flickering timescale $\sim 10^5$ years (Schawinski et al. 2015).

From the quantitative estimations, we show that the AGN outflows can remove the ionized gas within R_{NLR} in a reasonably short timescale, implying that star formation within ~ 1 kpc of AGN can be affected by AGN outflows. In Section 4.4, for example, we find that $\sim 30\%$ of AGNs with a disk are AGN-type disks, which is possibly affected by AGN photoionization. The higher $D_n(4000)$ and smaller $H\delta_A$ of the AGNs with AGN-type disks indicate a relatively low star-formation rate within the central kpc of the AGNs. We do not find, however, any differences between the AGNs with AGN-type and SF-type disks in terms of outflow energetics (Figures 23, 24, and 25).

Nonetheless, the most kinematically energetic AGNs of our sample, i.e., J0952+1937 and J1520+0757, may provide an insight into AGN feedback. For example, J1520+0757 has no detectable rotational feature in $H\alpha$, residing in the ‘‘green valley’’ with $\log \text{SSFR} = -10.9 \text{ yr}^{-1}$. On the other hand, J0952+1937 has a SF-type disk and harbors on-going star formation with $\log \text{SSFR} = -9.5 \text{ yr}^{-1}$ (see Figure 19). If the outflows in these AGNs are powerful enough to affect the star formation in the host galaxy, their different SSFRs are possibly due to different geometry of outflows with respect to the star-forming disk. This speculation can be tested using high spatial resolution IFU observations combined with a proper modeling of a mixed kinematics of outflows and disk rotation. Alternatively, the outflows may not be powerful enough to immediately quench the star formation in the host galaxy, although the ionized gas shows evidence of powerful outflows. Recent numerical simulations show the inefficiency of AGN outflows in quenching star formation, because the outflows are mostly affecting ionized gas, rather than dense molecular gas (e.g., Gabor & Bournaud 2014). This scenario can be tested whether the object shows outflow features in molecular gas as well as ionized gas via, e.g., ALMA observations.

Do AGN outflows also affect star formation on galactic scales (~ 10 kpc)? From our results, it would be difficult for our intermediate-luminosity AGNs, because of the steeply decreasing energy and momentum as a function of distance (see Section 5.1). Also, Karouzos et al. (2016b) showed that $\sim 90\%$ of outflow energy and momentum are within a $\sim 1\text{--}2$ kpc region ($\sim R_{\text{out}}$) in type 2 AGNs, implying that energy injected by AGN outflows would become smaller and eventually negligible at larger distance, e.g., ~ 10 kpc, for the AGN luminosities of our sample.

In Section 4.4, we find that the AGNs with SF-type disks are located on the main sequence of star-forming galaxies, while the AGNs with AGN-type disks are below the main sequence. The global SSFR of host galaxies of the AGNs with AGN-type disks is on average ~ 1 order of magnitude smaller than that in the AGNs with SF-type disks. Does the low SSFR in the sample of AGN-type disks support the AGN feedback in galactic scales? By considering that the AGNs with AGN-type disks are on average a factor of ~ 3.5 more

massive than the AGNs with SF-type disks (see Section 4.4), it is difficult to conclude that the low SSFRs support the galactic scale AGN feedback, although it is a plausible scenario. It is because such low SSFRs in massive galaxies can also be accounted for alternative quenching mechanisms, e.g., environmental quenching (e.g., Smith et al. 2012; Peng et al. 2015). More IFU-observed samples within similar mass scales may provide a hint for the primary quenching mechanism.

7. SUMMARY & CONCLUSION

Using the Magellan/IMACS-IFU and the VLT/VIMOS-IFU, we obtained the spatially resolved kinematics of ionized gas in the NLR for a luminosity-limited sample of 20 local type 2 AGNs, which are selected from a large sample of $\sim 39,000$ type 2 AGNs from SDSS DR7 (Woo et al. 2016), based strong outflow signatures, i.e., velocity dispersion $> 300 \text{ km s}^{-1}$ and/or large velocity offset $> 100 \text{ km s}^{-1}$ in [O III], with [O III] luminosity $\log L_{[\text{O III}]} > 41.5 \text{ erg s}^{-1}$. These AGNs are arguably best suited for studying AGN outflows. Here we summarize the main results.

- By performing a decomposition on the emission-line profile, we successfully obtained the flux and kinematic maps of the narrow- and the broad components of the [O III] and $H\alpha$ lines. The broad components in both [O III] and $H\alpha$ represent the non-gravitational kinematics, i.e., gas outflows, while the narrow components, especially in $H\alpha$, represent the gravitational kinematics.

- We measured the photometric size of the NLR (R_{NLR}) based on the [O III] flux distribution. By combining our sample and 29 luminous quasars from the literature, we obtained the photometric size-luminosity relation as $R_{\text{NLR}} \propto L_{[\text{O III}]}^{0.41}$, which is consistent with the results from the literature (e.g., Schmitt et al. 2003; Liu et al. 2013a).

- We obtained the outflow size (R_{out}) based on the spatially resolved [O III] kinematics as Karouzos et al. (2016a). We found no clear outflow size-luminosity relation, presumably due to the dynamical timescale of the outflows ($\sim 10^6$ years).

- By using the integrated spectra within R_{NLR} , we estimated the physical quantities of the outflow energetics. The estimated ionized gas mass is $(1.0\text{--}38.5) \times 10^5 M_{\odot}$ while the mean mass outflow rate \dot{M}_{out} is $4.6 \pm 4.3 M_{\odot} \text{ yr}^{-1}$, which is factor of ~ 260 higher than the mean $\dot{M}_{\text{acc}} \sim 0.02 \pm 0.01 M_{\odot} \text{ yr}^{-1}$. The result implies powerful mass loading of the AGN outflows by the ISM (e.g., Veilleux et al. 2005; Barbosa et al. 2009).

- The majority (18 out of 20) of AGNs have relatively low energy injection rate, which is about $0.8 \pm 0.6\%$ of L_{bol} , and also have relatively low momentum flux, which is about $\sim 5.4 \pm 3.6 \times L_{\text{bol}}/c$. Both the energy injection rate and the momentum flux correlate, in general, with L_{bol} . The estimated outflow parameters are consistent with the expectations from the energy-conserving outflow scenario with outflow velocities of $\sim 0.01\text{--}0.3c$ near the accretion disk (e.g., Faucher-Giguère & Quataert 2012). However, we find no supporting evidence for instantaneous quenching of the star formation due to the outflows.

We thank the anonymous referee for his/her valuable comments and suggestions. The work of HJB was supported by NRF (National Research Foundation of Korea) Grant funded by the Korean Government (NRF-2010-Fostering Core Leaders of the Future Basic Science Program). JHW acknowledges

the support by the NRF grant funded by the Korea government (No. 2016R1A2B3011457 and No. 2010-0027910). This work is based on observations made with ESO Telescopes at the La Silla Paranal Observatory under program ID 091.B-0343(A) (PI: Flohic), and data gathered with the 6.5 meter Magellan Telescopes located at Las Campanas Observatory, Chile. This work is also supported by K-GMT Science Program ID GN-2015A-Q-204 (PI:Woo) of Korea Astronomy and Space Science Institute (KASI). Based on observations obtained at the Gemini Observatory processed using the Gemini IRAF package, which is operated by the Association of Universities for Research in Astronomy, Inc., under a cooperative agreement with the NSF on behalf of the Gemini partnership: the National Science Foundation (United States), the National Research Council (Canada), CONICYT (Chile), Ministerio de Ciencia, Tecnología e Innovación Productiva (Argentina), and Ministério da Ciência, Tecnologia e Inovação (Brazil).

REFERENCES

- Abazajian, K. N., Adelman-McCarthy, J. K., Agüeros, M. A., et al. 2009, *ApJS*, 182, 543
- Bae, H.-J., & Woo, J.-H. 2014, *ApJ*, 795, 30
- . 2016, *ApJ*, 828, 97
- Baldwin, J. A., Phillips, M. M., & Terlevich, R. 1981, *PASP*, 93, 5
- Barbosa, F. K. B., Storch-Bergmann, T., Cid Fernandes, R., Winge, C., & Schmitt, H. 2009, *MNRAS*, 396, 2
- Bennert, N., Falcke, H., Schulz, H., Wilson, A. S., & Wills, B. J. 2002, *ApJ*, 574, L105
- Boroson, T. 2005, *AJ*, 130, 381
- Brinchmann, J., Charlot, S., White, S. D. M., et al. 2004, *MNRAS*, 351, 1151
- Cappellari, M., & Emsellem, E. 2004, *PASP*, 116, 138
- Choi, E., Ostriker, J. P., Naab, T., Oser, L., & Moster, B. P. 2015, *MNRAS*, 449, 4105
- Cicone, C., Maiolino, R., Sturm, E., et al. 2014, *A&A*, 562, A21
- Crenshaw, D. M., Schmitt, H. R., Kraemer, S. B., Mushotzky, R. F., & Dunn, J. P. 2010, *ApJ*, 708, 419
- Croton, D. J., Springel, V., White, S. D. M., et al. 2006, *MNRAS*, 365, 11
- Davies, R. L., Groves, B., Kewley, L. J., et al. 2016, *MNRAS*, 462, 1616
- Faucher-Giguère, C.-A., & Quataert, E. 2012, *MNRAS*, 425, 605
- Fischer, T. C., Crenshaw, D. M., Kraemer, S. B., & Schmitt, H. R. 2013, *ApJS*, 209, 1
- Fischer, T. C., Crenshaw, D. M., Kraemer, S. B., et al. 2015, *ApJ*, 799, 234
- Fischer, T. C., Crenshaw, D. M., Kraemer, S. B., Schmitt, H. R., & Turner, T. J. 2014, *ApJ*, 785, 25
- Gabor, J. M., & Bournaud, F. 2014, *MNRAS*, 441, 1615
- Greene, J. E., & Ho, L. C. 2005, *ApJ*, 627, 721
- Greene, J. E., Zakamska, N. L., & Smith, P. S. 2012, *ApJ*, 746, 86
- Hainline, K. N., Hickox, R., Greene, J. E., Myers, A. D., & Zakamska, N. L. 2013, *ApJ*, 774, 145
- Heckman, T. M., Kauffmann, G., Brinchmann, J., et al. 2004, *ApJ*, 613, 109
- Hopkins, P. F., Hernquist, L., Cox, T. J., et al. 2006, *ApJS*, 163, 1
- Horne, K. 1986, *PASP*, 98, 609
- Husemann, B., Kamann, S., Sandin, C., et al. 2012, *A&A*, 545, A137
- Husemann, B., Wisotzki, L., Sánchez, S. F., & Jahnke, K. 2013, *A&A*, 549, A43
- Husemann, B., Humphrey, A., Roche, N., et al. 2014, *MNRAS*, 443, 755
- Karouzos, M., Woo, J.-H., & Bae, H.-J. 2016a, *ApJ*, 819, 148
- . 2016b, *ApJ*, 833, 171
- Kauffmann, G., & Heckman, T. M. 2009, *MNRAS*, 397, 135
- Kennicutt, R. C. J. 1998, *ARA&A*, 36, 189
- King, A., & Pounds, K. 2015, *ARA&A*, 53, 115
- Kormendy, J., & Ho, L. C. 2013, *ARA&A*, 51, 511
- Liu, G., Zakamska, N. L., Greene, J. E., Nesvadba, N. P. H., & Liu, X. 2013a, *MNRAS*, 430, 2327
- . 2013b, *MNRAS*, 436, 2576
- Maiolino, R., Gallerani, S., Neri, R., et al. 2012, *MNRAS*, 425, L66
- Marin, F. 2014, *MNRAS*, 441, 551
- Markwardt, C. B. 2009, *Astronomical Data Analysis Software and Systems XVIII ASP Conference Series*, 411, 251
- Mullaney, J. R., Alexander, D. M., Fine, S., et al. 2013, *MNRAS*, 433, 622
- Müller-Sánchez, F., Prieto, M. A., Hicks, E. K. S., et al. 2011, *ApJ*, 739, 69
- Nesvadba, N. P. H., Lehnert, M. D., Eisenhauer, F., et al. 2006, *ApJ*, 650, 693
- Netzer, H. 2009, *MNRAS*, 399, 1907
- Osterbrock, D. E., & Ferland, G. J. 2006, *Astrophysics of gaseous nebulae and active galactic nuclei*
- Park, D., Kelly, B. C., Woo, J.-H., & Treu, T. 2012, *ApJS*, 203, 6
- Peng, Y., Maiolino, R., & Cochrane, R. 2015, *Nature*, 521, 192
- Riffel, R. A., Storch-Bergmann, T., & Riffel, R. 2014, *ApJ*, 780, L24
- Rupke, D. S., Veilleux, S., & Sanders, D. B. 2005, *ApJ*, 632, 751
- Rupke, D. S. N., & Veilleux, S. 2011, *ApJ*, 729, L27
- Sánchez-Blázquez, P., Peletier, R. F., Jimenez-Vicente, J., et al. 2006, *MNRAS*, 371, 703
- Sandin, C., Becker, T., Roth, M. M., et al. 2010, *A&A*, 515, A35
- Schawinski, K., Koss, M., Berney, S., & Sartori, L. F. 2015, *MNRAS*, 451, 2517
- Schmitt, H. R., Donley, J. L., Antonucci, R. R. J., et al. 2003, *ApJ*, 597, 768
- Schnorr-Müller, A., Storch-Bergmann, T., Nagar, N. M., & Ferrari, F. 2014, *MNRAS*, 438, 3322
- Shen, Y., & Ho, L. C. 2014, *Nature*, 513, 210
- Silk, J., & Rees, M. J. 1998, *A&A*, 331, L1
- Smith, R. J., Lucey, J. R., Price, J., Hudson, M. J., & Phillipps, S. 2012, *MNRAS*, 419, 3167
- Tombesi, F., Meléndez, M., Veilleux, S., et al. 2015, *Nature*, 519, 436
- Veilleux, S., Cecil, G., & Bland-Hawthorn, J. 2005, *ARA&A*, 43, 769
- Wang, J., Mao, Y. F., & Wei, J. Y. 2011, *ApJ*, 741, 50
- Woo, J.-H., Bae, H.-J., Son, D., & Karouzos, M. 2016, *ApJ*, 817, 108
- Zhang, K., Dong, X.-B., Wang, T.-G., & Gaskell, C. M. 2011, *ApJ*, 737, 71
- Zubovas, K., & King, A. 2012, *ApJ*, 745, L34
- Zubovas, K., & Nayakshin, S. 2014, *MNRAS*, 440, 2625

APPENDIX

ADDITIONAL FIGURES

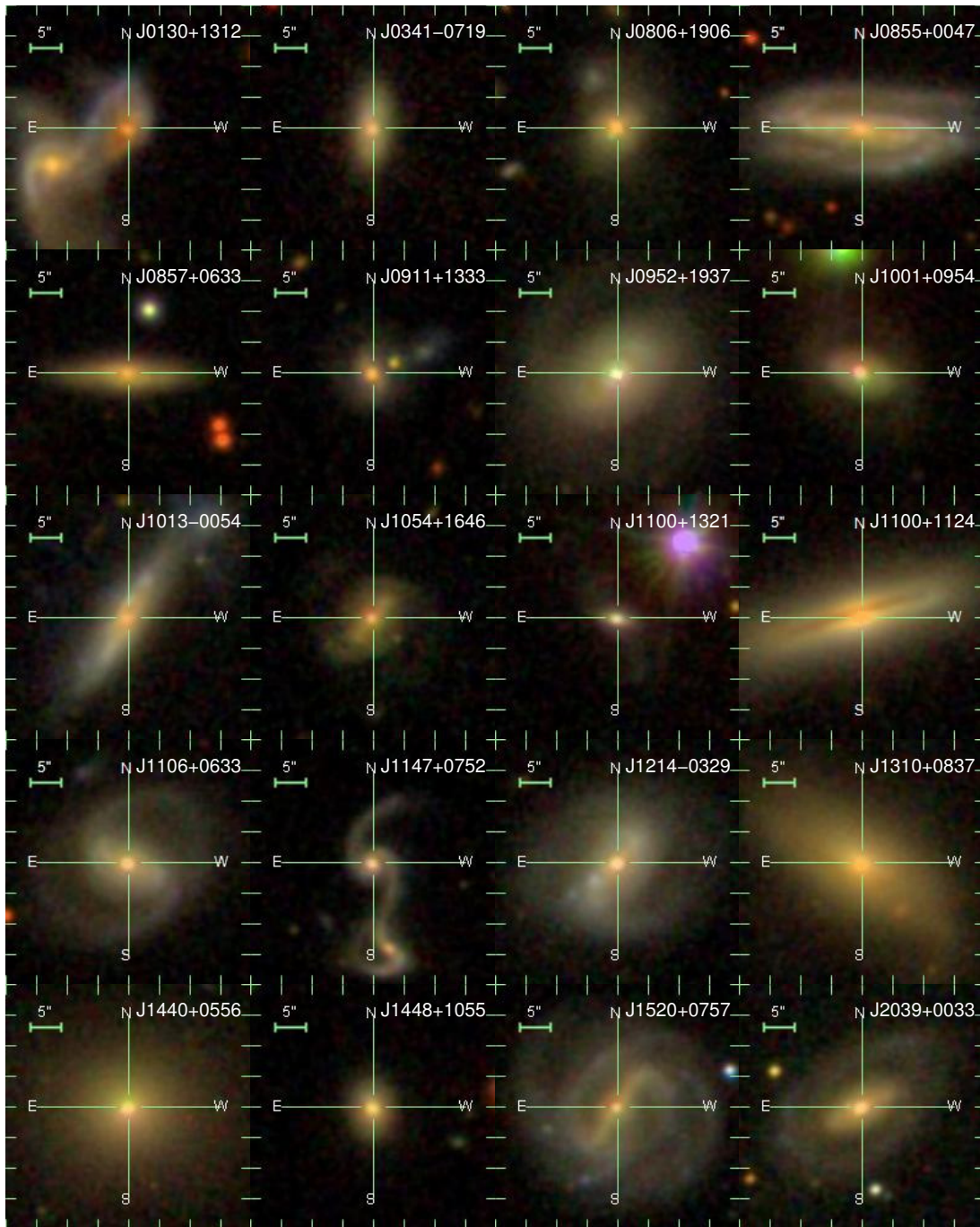


Figure A.1. SDSS *gri*-composite images ($40'' \times 40''$) of the 20 AGNs listed in accending R.A. from top-left to bottom-right. The name of the AGN is shown at the top-right corner of each image.

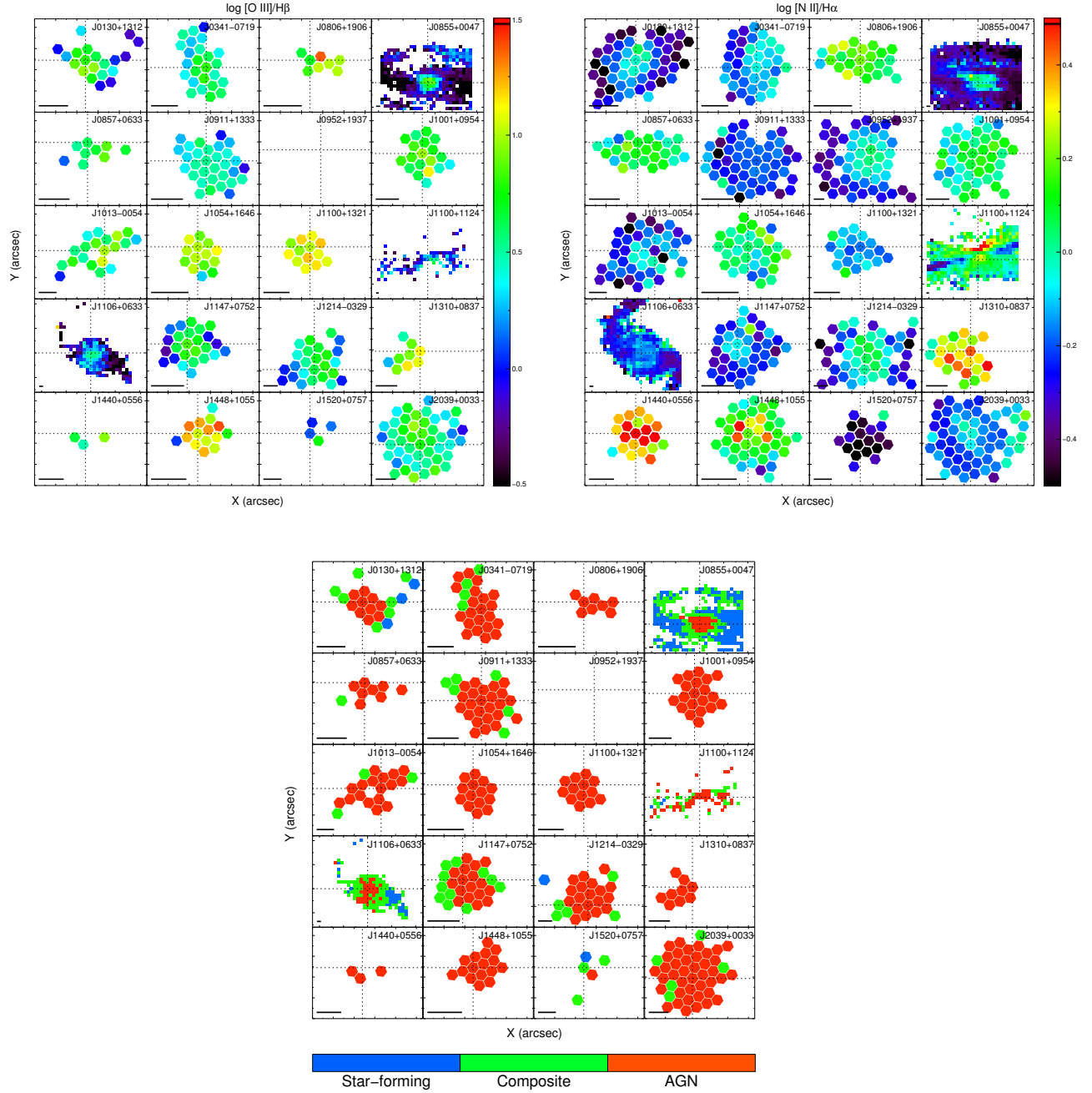


Figure A.2. The maps for the emission-line ratios of $[O\ III]/H\beta$ (top-left) and $[N\ II]/H\alpha$ (top-right), and the emission-line diagnostics (bottom). The major ticks in both x- and y-axes represent $1''$ for the Magellan targets, while the major ticks denote $5''$ for the VLT targets, i.e., J0855+0047, J1100+1124, and J1106+0633. The AGNs are listed in order of ascending R.A. from top-left to bottom-right as in Figure A.1. We note that J0952+1937 has no maps either $[O\ III]/H\beta$ nor in emission-line diagnostics since the $H\beta$ line is in the gap between the CCDs.